THESIS

UNMANNED AERIAL SYSTEMS FOR FOREST STRUCTURE MAPPING: ASSESSMENTS OF AREA-BASED AND INDIVIDUAL TREE MONITORING

Submitted by

Matthew Creasy

Department of Forest and Rangeland Stewardship

In partial fulfillment of the requirements

For the Degree of Master of Science

Colorado State University

Fort Collins, Colorado

Summer 2020

Master's Committee:

Advisor: Wade T. Tinkham

Chad Hoffman
Jody Vogeler

ABSTRACT

UNMANNED AERIAL SYSTEMS FOR FOREST STRUCTURE MAPPING: ASSESSMENTS OF AREA-BASED AND INDIVIDUAL TREE MONITORING

Characterization of forest structure is important for management-related decision making, especially in the wake of disturbance. Increasingly, observations of forest structure are needed at both finer resolution and across greater extents in order to support managers in meeting spatially explicit objectives. Current methods of acquiring forest measurements can be limited by a combination of time, expense, and either extent or temporal resolution. Drone or UAS-based photogrammetry provides an airborne method of forest structure data acquisition at a significantly lower cost and time commitment when compared to existing methods of such as airborne laser scanning (LiDAR). A growing body of literature confirms UAS-based photogrammetry models can be as detailed as conventional LiDAR models. However, there exists a knowledge gap in best practice for data acquisition parameters and assessment of accurate characterization within forest photogrammetry. The following two chapters utilize large stem mapped sites to fill that knowledge gap by 1) systematically testing the effects of UAS flight speed and altitude on plot-based aboveground biomass modeling through photogrammetry and 2) evaluating several algorithms for detecting individual tree locations and characterizing crown areas. Results show a strong positive relationship between flight altitude and aboveground biomass modeling, with all UAS flights evaluated above 80 m altitude, providing better results (2-24% more variance explained) than contemporary LiDAR

modeling strategies. Additionally, results demonstrate that the probability of detecting individual trees decays moving from the dominant overstory to suppressed trees, corresponding to >97% at the top of the canopy and decreasing to 67% for trees in the understory. Our results indicate the potential for UAS photogrammetry to produce highly detailed maps of forest biomass, as well as capture variation of forest structure through the detection of trees and tree groups. Such high-resolution data has the potential to become a much-needed tool for monitoring forest structures to inform spatially explicit management objectives. Additionally, these studies reinforced how UAS photogrammetry can provide low-cost repeat monitoring of forest conditions.

ACKNOWLEDGEMENTS

I would firstly like to thank my advisor, Dr. Wade Tinkham, for his willingness to take me on as a student and his incredible guidance throughout this process.

I would also like to thank my friends & family for their support and patience with my return to school in pursuit of a deeper fulfillment.

A special thank you to my mom for supporting me from afar and keeping me grounded.

This work would not have been possible without Neal Swayze, whose writing, knowledge, and guidance in the FAA Part 107 process was invaluable.

Thank you to Alex Weissman all the field crews that helped gather the data we needed.

Lastly, I would like to thank my dog, Gus, for holding me accountable while I worked from home the last semester.

DEDICATION

For my Father, J.W. Creasy, who taught me the value of an inquisitive mind.

TABLE OF CONTENTS

LIST OF TABLES

LIST OF FIGURES

Chapter 1: INFLUENCE OF UAS FLIGHT ALTITUDE AND SPEED ON ABOVEGROUND BIOMASS PREDICTION

1.1 Introduction

Forests provide a variety of natural and societal benefits, with complex interactions governing recruitment, growth, and mortality processes across multiple-scales (Pan et al., 2013; Anderegg et al., 2015). In order to maximize these benefits, forest managers are increasingly acknowledging the need to monitor and manage forest structure at spatio-temporal scales, which accurately describe the spatial variability in forest dynamics (Briggs et al., 2017). Such forest management decisions require data that represent the continuous nature of ecological phenomena such as structures supportive of wildlife habitat (Vogeler et al., 2016). Complex ecological processes in forests that govern recruitment, growth, and mortality occur at the scale of tree-tree interactions (Dickinson et al., 2016). Traditional forest inventory methods, typically consisting of plot-based networks of *in situ* measurements, are limited in their ability to represent these cross-scale ecological processes and forest spatial arrangements (Lutz, 2015). Despite the need for more continuous methods for characterizing forest structure across landscapes, the acquisition of plot networks of sufficient spatial and temporal resolution is limited by financial constraints (Torresan et al., 2016).

The development of aerial Light Detection and Ranging (LiDAR) techniques for providing spatially continuous observations of forest structure has revolutionized the incorporation of landscape-level information in the decision-making process (Hudak et al., 2009; Nelson, 2013). LiDAR has been shown to produce reliable area-based estimates of forest density (i.e., basal

area per hectare; Hudak et al., 2006) and biomass (Bouvier et al., 2015), while also providing reasonable individual tree observations of height and volume (Tinkham et al., 2016). Despite these recent innovations, LiDAR data acquisition can be cost prohibitive as the price of crew mobilization alone starts at >$20,000 (Hummel et al., 2011). This price can preclude low-productivity forest ecosystems from using the technology, as the value of the forest resource must justify the expense of data acquisition for effective management. Smaller land management organizations, which are unable to justify the cost, are commonly prevented from employing these techniques to inform their planning process. Larger organizations that can bear the initial cost may still find it impractical to obtain LiDAR at a temporal resolution suitable for monitoring forests responding to combinations of climatic, disturbance, or management influences (Mitchell et al., 2017). As ecological management drives increased demand for frequent, fine-scale observations of forest structure, new methods of forest structure characterization require further development.

Unmanned Aerial Systems (UAS) are uniquely positioned to meet the demand for fine-scale observations of forest structure by providing spatially-continuous observations at a higher temporal resolution. Professional grade UAS have recently become more accessible to consumers with entry costs under $2,000. Despite the low price point, UAS typically have high-accuracy GPS receivers, automated inertial navigation systems, object detection/avoidance, and improved sensors for very high-resolution (VHR; < 10 cm) remote sensing (Torresan et al., 2017). This combination of technologies is ideal for photogrammetry, which requires high-resolution, spatially-accurate images. Autopilot technology allows users with minimal technical training to operate UAS for repeatable photogrammetry surveys, with commonly used flight

planning applications, including PrecisionMapper, Pix4Dcapture, DroneDeploy, DJI Ground Station Pro, and Altizure. UAS-mounted sensors are starting to surpass the spatial resolution previously only seen in aircraft-based remote sensing, while integrated control and navigation systems are becoming better equipped to maximize the sensor's potential. Preliminary studies have evaluated both fixed-wing and multirotor UAS platforms equipped with a range of sensors for data collection, including consumer and professional grade RGB compact camera systems, among others (Wallace et al., 2016; Fritz et al., 2013; Zarco-Tejada et al., 2014; Webster et al., 2018; Thiel & Schmullius, 2016). The high-cost and temporal resolution limitations of LiDAR are where UAS can fill data needs for forest management organizations; UAS cost orders of magnitude less than aircraft-based LiDAR acquisitions and can be flown as often as favorable conditions are met. Despite their potential, UAS are currently limited in the area that can be covered in a single acquisition by relatively short flight times due to battery capacity and governmental regulations requiring pilots to maintain a line of sight or visual contact with the platform at all times. Additionally, UAS are known to be impacted by changing light conditions during acquisition (O'Connor et al., 2017) and high winds, which can lead to errors in image matching (Iglhaut et al., 2019). While UAS have limitations, the low cost of deployment and the ability to collect VHR data demonstrates a niche for more frequent monitoring at the stand-scale that UAS can provide.

Over the last decade, numerous studies have utilized UAS to generate VHR two-dimensional orthomosaic maps (Torrez-Sanchez et al., 2015; Fraser & Congalton, 2018) and three-dimensional point clouds of forest structure and terrain using various Structure from Motion (SfM) processing algorithms (Thiel & Schmullius, 2016; Frey et al., 2018). SfM

algorithms identify common points within overlapping images and, through a geometric process utilizing the position and rotation of captured images, a three-dimensional point cloud is generated (Frey et al., 2018). Due to the high degree of overlap, SfM point clouds can have data densities in excess of 1,000 points m^{-2} compared to LiDAR's common 4-30 points m^{-2}, and therefore have the potential to better capture the fine-scale complexity of forest structure than LiDAR. Additionally, recent studies have found that including UAS orthomosaic spectral data in SfM modeling resulted in it being a significant parameter in 80% of models predicting forest biomass (Domingo et al., 2019).

Early UAS research has revealed that the accuracy of forest structure estimates varies based on data acquisition parameters such as forward and side image overlap, flight altitude, and speed. Dandois et al. (2015) demonstrated that increasing the levels of forward and side overlap until at least 80% led to improved location and height accuracies in forested environments. When controlling forward and side overlap separately, Seifert et al. (2019) found that maintaining high (>90%) forward overlap with lower side overlap (~70%) provided a balance between data accuracy, flight time, area coverage, and data processing time. Most studies have concluded that forward overlap should be maximized as it does not impact flight time or the area covered in a single acquisition. In contrast, side overlap can be reduced depending on data objectives to achieve a larger acquisition area.

Several studies have evaluated the influence of flight altitude on data quality and forest structure characterization accuracy with conflicting results. Seifert et al. (2019) found that low altitude flights within 15-20 m of the vegetation canopy resulted in significantly more image registration points with improved precision. However, Fraser & Congalton (2018) found that

flying at 100 m above the vegetation canopy provided the best image alignment. Additionally, Torres-Sánchez et al. (2015) found no significant impact of altitude on object-based canopy parameter extraction. Faced with these conflicting results, it is necessary to standardize flight acquisition parameters for a consistent interpretation of UAS survey results across different environments and methods. Additionally, each of these studies evaluated how altitude impacted image alignment for study areas at similar forests to understand the role of forest structure characterization on end-product forest measurements.

While these results indicate a range of optimal parameters for UAS image alignment within different vegetation types, significant knowledge gaps exist for both guiding future image acquisition and the translation of parameter optimization to the accuracy of UAS-based forest structure characterization. There is, therefore, a significant need for systematic testing of flight survey parameters in order to quantify the impact of forest structure on SfM-derived point clouds (Torres-Sánchez et al., 2015).

This study seeks to examine how flight altitude and speed impact UAS model reliability in explaining forest biomass compared to standard aerial LiDAR modeling strategies across a range of forest structures found in ponderosa pine (*Pinus ponderosa var. scopulorum* Dougl. Ex Laws.) dominated forests. Specifically, comparisons of variance explained, and precision between UAS- and LiDAR-based models of forest biomass will be examined through their response to flight altitude and speed. Additionally, this analysis will investigate how segmentation of SfM point clouds based on spectral indices impacts model performance. The effects of flight altitude and speed will be discussed in terms of data collection, processing times, and data density.

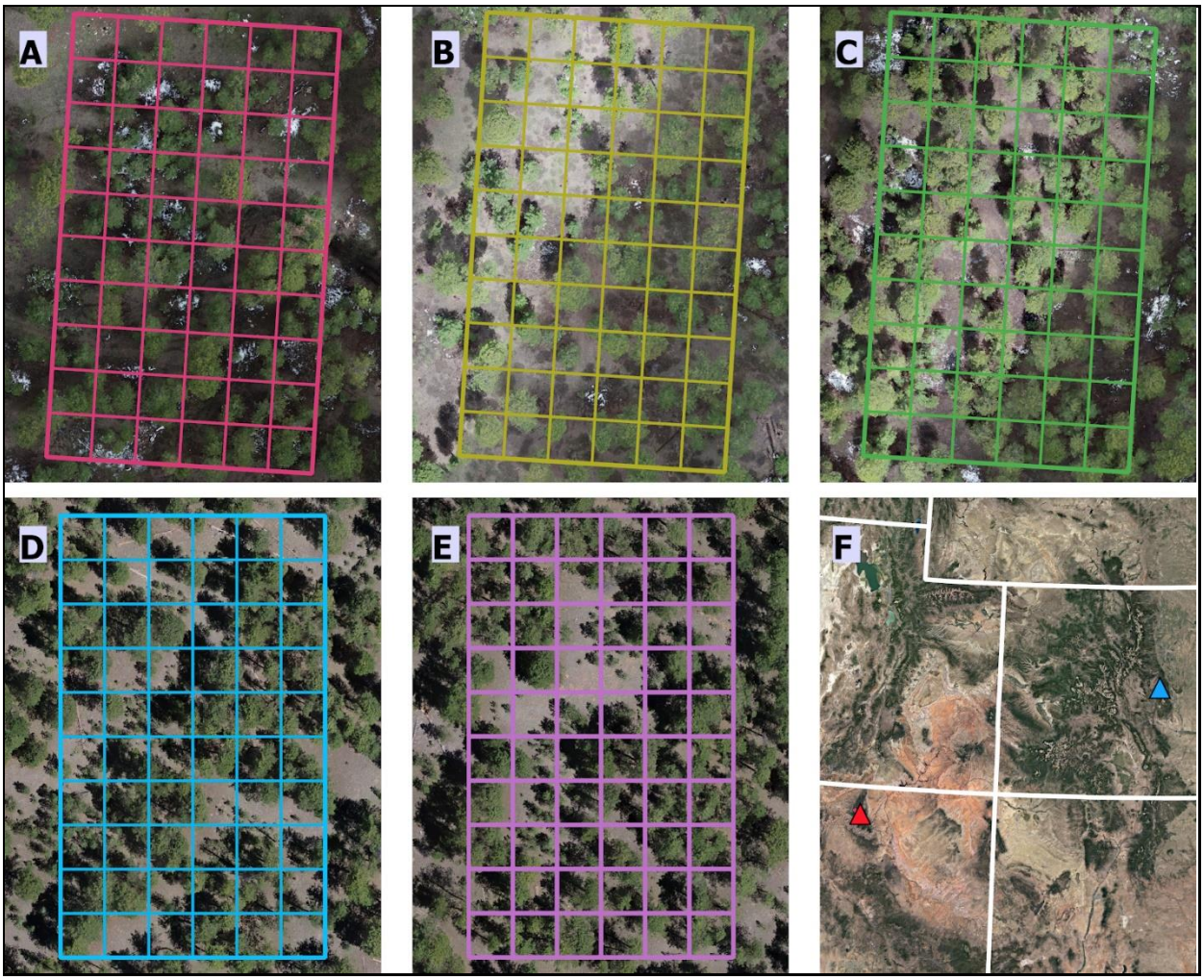

Figure 1.1. Five 60 x 100 m study areas at the Kaibab National Forest in Northern Arizona (KNF1: A, KNF2: B, KNF3: C) and Manitou Experimental Forest in Central Colorado (MEF1: D, MEF2: E), with the location of KNF study area (red) and MEF study area (blue) displayed in panel F.

1.2 Methods

1.2.1 Study Area and Field Data

This study was conducted across two ponderosa pine dominated forests with existing aerial LiDAR and stem mapped forest inventories in the central Rocky Mountains (Figure 1.1). Within these forested areas, five study units were selected to represent a range of forest densities. The first forest is the N1 forest dynamics site located within the Manitou

Experimental Forest on the Pike-San Isabel National Forest in Colorado, about 40 km northwest of Colorado Springs. The average elevation is 2,500 m, with a mild slope (< 5%) to the southeast. This location provides an example of a typical human-influenced montane ponderosa pine forest, as it was selectively logged between 1880 and 1886 (Boyden et al., 2005). After logging, the forest was undisturbed with no significant fire since 1846 and only minor mountain pine beetle disturbance in the late 1970's. During the 140 years following harvest activities, the N1 forest has since experienced several regeneration pulses that have led to varying forest densities, with minor components of Douglas-fir (*Pseudotsuga menziesii* (Mirb.) Franco var. *glauca* (Beissn.) Franco) and blue spruce (*Picea pungens* Engelm.) in the understory, Native grasses and a few low growing woody shrubs comprise the sparse understory vegetation. To control for variation in forest densities during testing, the N1 forest was divided into two separate study units for UAS data acquisition, hereafter referred to as MEF1 and MEF2 (Table 1.1).

Table 1.1. Forest stand structure at the Manitou Experimental Forest (MEF) and Kaibab National Forest (KNF) study units, reported as mean (standard deviation) of 0.01 ha sampling unit.

Study Area	QMD (cm)	Max Tree Height (m)	Basal Area (m^2 ha^{-1})	Trees ha^{-1}	AGB* (tons ha^{-1})
KNF1	30.3 (14.8)	15.9 (8.0)	26.9 (22.0)	300 (197)	90.6 (51.1)
KNF2	31.2 (22.0)	14.9 (9.6)	21.2 (22.1)	200 (186)	80.7 (55.6)
KNF3	32.9 (14.6)	22.2 (6.2)	44.5 (29.2)	626 (446)	128.9 (54.7)
MEF1	21.7 (11.8)	17.5 (6.6)	24.8 (15.9)	931 (806)	90.2 (34.9)
MEF2	23.5 (11.3)	17.1 (5.4)	26.9 (17.4)	701 (407)	93.4 (35.1)

* aboveground biomass calculated using Jenkins et al., 2003

The Lookout Canyon forest dynamics site is located in the Kaibab National Forest in northern Arizona, approximately 65 km southeast of Kanab, Utah, at an elevation of approximately 2,400 m. The forest is primarily composed of ponderosa pine and was divided into three 4-hectare stands for thinning, including a control stand and two stands thinned to 9.2 and 13.8 m^2 ha^{-1} of basal area in 1993 (Table 1.1), hereafter KNF1, KNF2, and KNF3. Following thinning, quaking aspen (*Populus tremuloides* Michx.) began reestablishing within the understory alongside considerable pulses of ponderosa pine regeneration. A prescribed fire in an adjacent stand escaped in 1999 and burnt through the understory killing more than 600 small diameter trees.

All trees taller than 1.37 m were stem mapped at each of the five study units using a grid of known survey locations. For each mapped tree, the species, diameter at breast height (1.37 m; DBH), and height was recorded. Stem mapping of the 60 x 100 m study units (0.6 ha) was completed in July 2018 for MEF1 and MEF2 and in May 2019 for KNF1, KNF2, and KNF3. The study stem maps were divided into 10 x 10 m (0.01 ha; n = 60) sampling units. Each sampling unit was analyzed separately in the Central Rockies variant (Keyser & Dixon, 2008) of the Forest Vegetation Simulator (Dixon, 2002) to determine total aboveground biomass (AGB). Biomass was estimated as metric tons ha^{-1} using allometries from Jenkins et al. (2003) as implemented in the Forest Vegetation Simulator.

1.2.2 UAS Data Acquisition

UAS image data was collected using a DJI Phantom 4 Pro (Dá-Jiang Innovations Science and Technology Co. Ltd., Shenzhen, China) multirotor equipped with a 20-megapixel (5472 x 3648 pixels) metal oxide semiconductor (CMOS) red-green-blue (RGB) sensor, with a fixed 8.8

mm focal length (Figure 1.2A). For all image acquisitions, the camera was set to infinity focus, with an aperture (F-stop) of 5.6, a shutter speed of 1/500s, and ISO values ranging from 100 to 200 depending on lighting conditions. The aircraft recorded geolocation (x, y, and z) and camera parameter values for each captured photo to a manufacturer-stated vertical accuracy of ±0.5 m and horizontal accuracy of ±1.5 m (https://www.dji.com/phantom-4-pro).

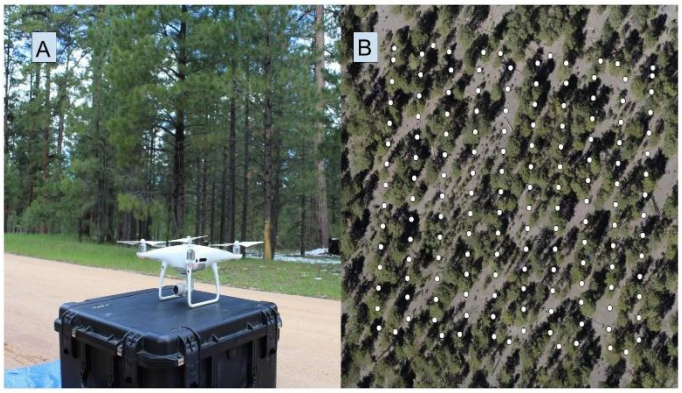

Figure 1.2. (A) DJI Phantom 4 Pro aircraft at KNF study area. (B) Conventional UAS survey depicting the automated route generated by Altizure. The white circles represent approximate camera capture locations for a flight 120 m above ground level.

Flight planning and execution were performed using Altizure version 4.6.8.193 (Shenzhen, China) for Apple iOS. The application was utilized to pre-program automated UAS flight paths with desired altitude, forward and side photo overlap, flight speed, exposure, aperture and shutter speed (Figure 1.2B). To better understand the optimal altitude for generating photogrammetric models of forest structure, 40 independent UAS flights were planned (8 acquisitions per study area) at randomly chosen altitudes ranging from 40 to 120 m above ground level. Three flight speeds were systematically assigned to each altitude, including 2, 3, and 4 m sec^{-1}. This study utilized a nadir camera angle, with 90% forward and 90% side photo overlap for all data acquisitions. This overlap combination was selected based on previous research that suggested that forward and side overlaps greater than 80% improved

image alignment, improved tree height estimation, and reduced understory occlusion in UAS surveys (Dandois et al., 2015; Frey et al., 2018).

An adaptive flight boundary methodology was used to maintain a constant number of flight lines and photo density or the number of photos viewing the same location at each of the desired altitudes. Initial testing showed that failing to increase flight boundary dimensions as altitude increases led to fewer flight lines and photos, resulting in reduced data density for the point cloud generation. In order to implement this methodology, 10% of the camera footprint (widths and lengths in meters) was determined across different altitudes and multiplied by 10 to ensure maximum photo density at the center of the study area. This resulted in flight boundaries varying between 80 x 110 m and 161 x 110 m at flight altitudes of 40 and 120 m, respectively. At the Kaibab study units, it was determined that three of the randomly assigned UAS surveys could not be completed due to concerns of collision with the canopy at the lowest altitudes (<45 m), resulting in a total of 37 flights.

All UAS surveys were flown between April and August 2019 and within three hours of solar noon to maintain a minimum solar angle of 50° from the horizon. All flights were conducted within the line of sight of the remote pilot in command with the assistance of a visual observer to comply with Part 107 Federal Aviation Administration regulations.

1.2.3 Ground Control Points

The methodology for ground control point (GCP) implementation followed the procedures outlined in the Australian Photogrammetry for Forest Inventory Planning Guide (Osborn et al., 2017). Ten high visibility ~0.2 m^2 GCPs were collected using a Trimble GeoXT (Trimble Inc., Sunnyvale, CA, USA) with SBAS real-time corrections for each of the five study

units with accuracies of <1 m. All points were placed to account for visibility from the air with the UAS. Four points were set as close to each corner as possible, one along each long edge and the remaining four points were distributed throughout the center (Figure 1.2). The GCPs were differentially corrected using Trimble Pathfinder Office software. GCPs were imported into ArcGIS 10.6.1 (ESRI Inc.; Redlands, CA, U.S.A.), and projection was defined as the WGS 1984 coordinate system to match the UAS imagery. Latitude, longitude, and altitude were then exported for use in georectifying the UAS imagery.

1.2.4 UAS Structure from Motion Point Cloud Generation Data Processing

Agisoft Metashape version 1.5.3 (www.agisoft.com; Agisoft LLC, St. Petersburg, Russia) was used to implement a SfM photogrammetry algorithm. SfM algorithms generate 3D point clouds by identifying image features and GCPs in each image and using these features to align the images in space. After these matches are found, a photogrammetric sparse bundle adjustment calculates the 3D location of each of the images in space using the camera parameters and the 3D geometry of the objects found within the images (Dandois et al., 2015). The Agisoft Metashape processing was implemented through a cloud server utilizing a 2.7 Ghz Intel Xeon E5 2686 V4 computer processor unit with two NVIDIA Tesla M60 graphics cards, and a total of 240 gigabytes of random-access memory.

The Agisoft Metashape workflow closely followed the processing methodology found in the Agisoft Photoscan user manual (Link, 2017), with the only departure including local testing of the dense cloud and depth filter settings. Using the MEF1 95 m acquisition, the 20 possible combinations of the Agisoft Metashape build dense cloud quality settings and depth filtering settings were tested on this photo dataset, resulting in 20 unique point clouds with different

point cloud densities and processing times. From this it was determined that SfM setting in Agisoft Metashape for forest reconstruction in this study would be set to High quality and Mild depth filtering as these settings provided a balance between data density and processing time and align with settings commonly used in other studies (Fraser & Congalton, 2018; Goldbergs et al., 2018). The full suite of selected Agisoft Metashape settings for image dataset processing is depicted in Appendix Table 1.1.

Each of the SfM point clouds were exported from Agisoft Metashape with UTM Zone 13N and 12N projections for Colorado and Arizona, respectively. CloudCompare version 2.10.1 (www.cloudcompare.org), a software designed for 3-dimensional point data comparison, was used to visually inspect each point cloud to ensure complete dense cloud reconstruction. Agisoft Metashape processing reports were also generated and checked to ensure similar processing errors across the point cloud models. Clouds with significant processing errors or incomplete reconstruction were reprocessed to ensure comparable accuracy and quality across the 37 surveys.

1.2.5 LiDAR Datasets

At the Manitou Experimental Forest sites aerial LiDAR data was acquired in August 2014 at a nominal point density of 5.74 points m^{-2}. Aerial LiDAR data for the Kaibab National Forest sites was acquired in the winter of 2012 at a nominal point density of 13.70 points m^{-2}. The time difference between the LiDAR acquisitions and the field inventory corresponds to average tree height growths of 0.5 m at MEF and 1.1 m at KNF, derived from prior site inventories. The LiDAR point clouds were cropped to the five study unit extents and used as an industry standard for comparing the accuracy of the UAS modeled forest biomass.

1.2.6 Point Cloud Processing

All 37 SfM UAS point clouds and the five aerial LiDAR point clouds were processed using LAStools version 1.2 (http://lastools.org). The LiDAR and SfM point clouds were initially clipped to a buffered extent of 90 m x 130 m to provide a margin around each of the five study areas and to prevent geometry irregularities known to occur at the edge of point clouds during processing. Point clouds were filtered to remove noise by selecting block minimum points and fitting a digital elevation model with a spline fit; points that fell below the digital elevation model were classified as noise and removed from further processing. The remaining points were classified as either ground or non-ground points.

After filtering and classification, each point cloud was clipped to the final 60 x 100 m study unit extent. Points classified as ground were extracted from each point cloud and visually compared to the LiDAR ground points in CloudCompare, revealing a slight Z-axis misalignment between the SfM and LiDAR datasets. This misalignment is attributed to low vertical precision in the GCPs from overstory trees, causing some degree of GPS satellite signal occlusion. There was minimal observed x- and y-axis misalignment between the SfM and LiDAR ground points, which suggested that the GCPs had high horizontal precision. This SfM ground point cloud misalignment was corrected using the iterative closest point - fine alignment tool to develop a custom transformation matrix for each SfM point cloud that was applied to the full SfM point cloud to align it with the LiDAR point cloud. Following geometric transformation, each SfM and LiDAR point cloud was height normalized against their classified ground points.

The SfM points clouds were further processed to investigate how segmentation of the points based on spectral indices impacts the prediction of forest biomass. To train the point

segmentation, all filtered and classified point clouds at a study site were merged using LAStools and loaded into CloudCompare. From the merged point cloud, 15 random samples each of canopy and stem (each containing 20,000-60,000 points) were manually extracted to ensure pure representation of both stem and canopy points. These classified stem and canopy point samples were imported to the R statistical programming language (R core Team, 2019) using the lidR package (Roussel & Auty, 2019). From each point sample, the red and green reflectance data was used to calculate the Normalized Green-Red Ratio (NGRR) using Equation 1.

$$NGRR = \frac{G_{band} - R_{band}}{G_{band} + R_{band}} \quad \text{[Equation 1]}$$

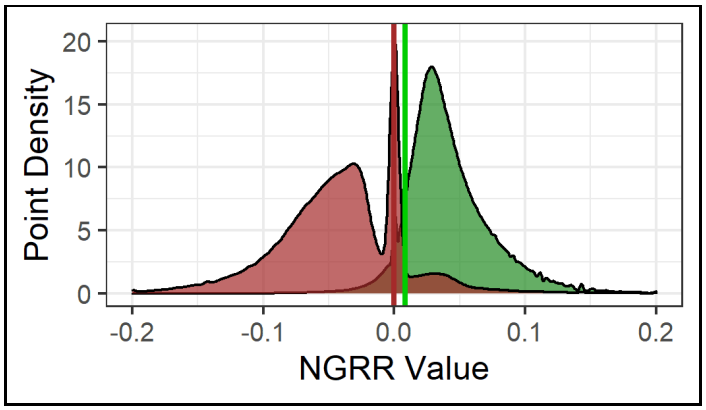

Figure 1.3. Example density plot of the canopy (green) and stem (red) NGRR values sampled from SfM point clouds at the MEF1 study area, where overlapping distribution segments are brown. Red and green vertical lines represent the 90th and 10th percentile of the stem and canopy values, respectively.

Visual inspection of density plots for the stem and canopy indexed points for each study site (Figure 1.3) showed segregation of NGRR values when the data was split with stem values less than their 90th percentile and canopy values greater than their 10th percentile. Across the five study units, the stem 90th percentile varied from -0.0096 to 0, and the canopy 10th percentile varied from 0 to 0.0747. These segmentation thresholds were used to segment the

SfM point clouds into three different categories for each of the 37 acquisitions: Stem, Canopy, and Standard, where Standard is the non-NGRR classified point cloud (Figure 1.4).

1.2.7 Forest Biomass Modeling

To develop models of aboveground biomass the three SfM point clouds for each of the 37 UAS acquisitions and the five LiDAR point clouds were processed using the lascanopy utility in LAStools. This function generated 21 point cloud distributional metrics for each of the 60 sampling units (Figure 1.1) that aligned with the FVS modeled AGB for each study unit. These distributional metrics included maximum, average, minimum, standard deviation of height, skewness, kurtosis, average square height, percentiles (5, 25, 50, 75, 90), bicentiles (5, 25, 50, 75, 90), vertical complexity index (0, 1, 2), and percent canopy cover.

At each site, the LiDAR point cloud distribution metrics were used to create baseline predictions of AGB using the randomForest package (Liaw and Wiener, 2002) of the R statistical programming language. In order to refine the number of predictors being used to model AGB, the Random Forest Model Selection tool (Murphy et al., 2010) was used to select the top five predictors in each model. The top five point cloud metrics for each dataset were used as predictor variables to model AGB using a series of random forest regressions with 10,000 trees each (Breiman, 2001), where the 60 sampling units were randomly divided into training observations (80% or n=48) and validation observations (20% or n=12). The same process for modeling AGB was repeated for each UAS data acquisition using the Standard SfM point cloud distribution metrics and then again with the point cloud distribution metrics combined for the Standard, Stem, and Canopy datasets, referred to as Standard + NGRR hereafter. In total, 74

UAS random forest models (37 Standard SfM and 37 Standard + NGRR SfM) were compared against the five LiDAR random forest models for the same respective study unit.

Figure 1.4. Example point clouds and density histograms for high biomass (top panels) and low biomass locations (bottom panels), including LiDAR (A and E), Standard SfM (B and F), Stem SfM (C and G), and Canopy SfM (D and H).

1.2.8 Model Evaluation

The 74 SfM random forest models were evaluated by relativizing them against their respective LiDAR random forest model through the calculation of percent change in model performance metrics of the Coefficient of Determination (ΔR^2; Equation 2), Root Mean Squared Error (ΔRMSE; Equation 3), and Mean Absolute Error (ΔMAE; Equation 4).

$$\Delta R^2 = \frac{SfM\ R^2_{ij} - LiDAR\ R^2_i}{LiDAR\ R^2_i} \times 100 \quad \text{Equation 2}$$

$$\Delta RMSE = \frac{SfM\ RMSE_{ij} - LiDAR\ RMSE_i}{LiDAR\ RMSE_i} \times 100 \quad \text{Equation 3}$$

$$\Delta MAE = \frac{SfM\ MAE_{ij} - LiDAR\ MAE_i}{LiDAR\ MAE_i} \times 100 \quad \text{Equation 4}$$

Where i denotes an individual study site, while j signifies the individual UAS acquisitions within that site. These relativized metrics should be interpreted as positive values of ΔR^2 indicating percentage improvement of the UAS model over the LiDAR model, while negative values of ΔRMSE and ΔMAE indicate percentage reductions in the UAS model compared to the LiDAR model. To standardize the effect of altitude on model performance across the five sites, the effect of altitude was also evaluated as a ratio ($A{:}L_H$; Equation 5) of altitude (A) compared to Lorey's Mean Height (L_H; Equation 6).

$$A{:}L_H = \frac{Altitude\ (m)}{L_H(m)} \quad \text{Equation 5}$$

$$L_H = \frac{\sum g \times h}{\sum g} \quad \text{Equation 6}$$

Where g is a tree's basal area (m^2) and h is a tree's height (m), meaning that L_H can be interpreted as the weighted height of the forest were a stand with more regeneration will see this value be less than the arithmetic mean. The model performance metrics ΔR^2, ΔRMSE, and ΔMAE were all evaluated as a function of altitude and L_H.

To evaluate the relationship between Standard UAS random forest model performance metrics with UAS data acquisition flight altitude and speed, linear mixed-effects regression was performed. In this analysis, the 37 combinations of UAS acquisition altitude and speed were treated as fixed effects, while the five study sites were treated as a random-effect. Additional covariates of stand-level forest structure and AGB were also evaluated for their influence on model performance. While testing for interactions, a stepwise procedure was used to identify the best subset of explanatory factors that minimized the Akaike Information Criterion (AIC). All regression was performed using lme4 packages (Bates et al., 2015) of the R statistical programming language.

Finally, after pooling the important point cloud distribution metrics from each random forest model, they were evaluated based on the proportion of models they appeared in. This analysis was extended to contrast the changes in important distribution metrics for the Standard SfM models with the Standard + NGRR SfM models.

1.3 Results

1.3.1 LiDAR AGB Model Performance

The five aerial LiDAR random forest model results for AGB varied across the study sites, with R^2 averaging 0.539 (range 0.424 - 0.666). However, R^2 values for the three MEF study sites were 0.129 higher than those for the two KNF study sites. Additionally, the KNF study sites had nearly twice as much variation in the 0.01 ha sampling units for AGB, basal area ha^{-1}, and max tree heights compared to the MEF sites (Table 1.1). Similar contrasts in model performance were found in RMSE, which ranged from 23.9 to 56.8 tons ha^{-1}, and MAE, which ranged from 15.8 to 55.1 tons per ha^{-1}. Variation in these metrics across the five study sites followed the same trend as the R^2 values.

1.3.2 Standard AGB Model Performance

Random forest AGB model performance for Standard UAS SfM parameters compared to LiDAR models of AGB varied across flight altitudes (Figure 1.5). The lowest altitude UAS acquisitions at each study site failed to reconstruct the vertical profile of the vegetation and provided substantially worse results compared to the LiDAR predictions (average ΔR^2 = -20.6%). For acquisitions that correctly generated SfM point clouds, the average ΔR^2 was 4.4%, with model performance generally improving with increased altitude. Linear mixed-effects modeling of ΔR^2 as a function of flight altitude and speed demonstrated a significant effect of flight

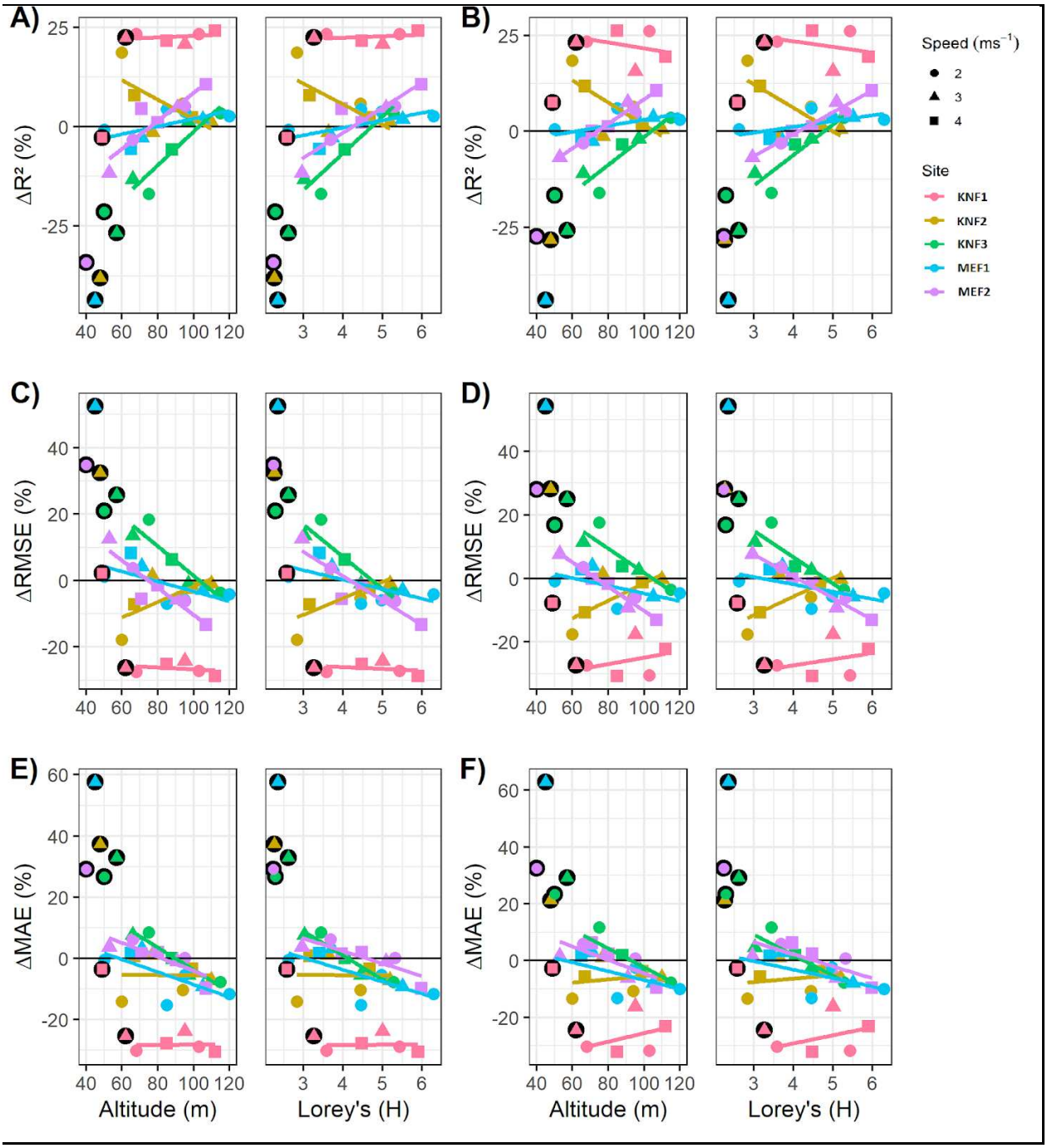

Figure 1.5. Comparison of Standard (panels A, C, & E) and Standard + NGRR (panels B, D, & F) AGB model performance metrics relativized to LiDAR, including percent ΔR^2 (panels A & B), ΔRMSE (C & D), and ΔMAE (E & F). The panel is split to show the influence of altitude above ground (left) and the ratio A:L_H (right). Points in black circles represent acquisitions that failed to reconstruct the forest canopy.

altitude on ΔR^2, but not flight speed (Table 1.2). Average ΔR^2 varied from nearly a 20% reduction in prediction performance at the lowest altitudes to nearly a 20% improvement in prediction performance over the LiDAR models at the highest altitudes (Figure 1.6). Similar improvements with increased altitude were seen for Standard UAS SfM models of AGB for ΔRMSE and ΔMAE (Figure 1.5). For models correctly generating SfM point clouds, the ΔRMSE and ΔMAE were reduced by 5.1% and 6.9%, respectively.

Table 1.2. Linear mixed-effects model of the influence of flight altitude and speed on change in aboveground biomass model R^2. The five study sites were treated as a random effect.

Parameter	Coefficient	Standard Error	t-value	p-value
Standard Flight Altitude				
Intercept	-30.272	10.401	-2.910	0.0067
Altitude (m)	0.403	0.082	4.908	<0.001
Speed (m s^{-2})	-0.574	2.325	-0.247	0.8068
Relativized Flight Altitude				
Intercept	-30.403	10.134	-3.000	0.0053
Lorey's Height	7.996	1.594	5.018	<0.001
Speed (m s^{-2})	-0.606	2.316	-0.261	0.7955

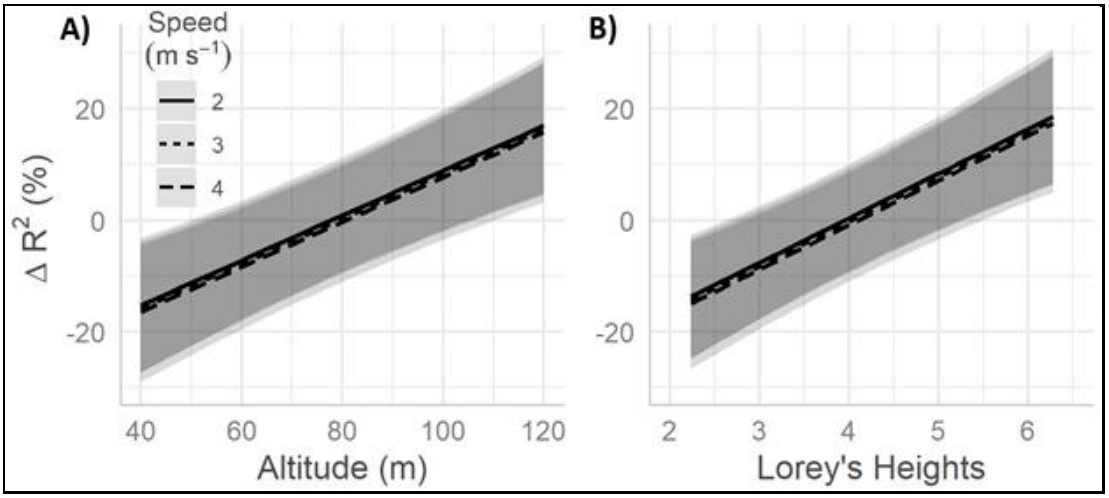

Figure 1.6. Linear mixed-effects model results for the 37 Standard SfM AGB models.

Standard UAS SfM parameters always resulted in improved model performance at the highest altitudes, with altitudes at which models began outperforming LiDAR models varying from ~80 to 100 m (Figure 1.5). Standardizing flight altitude as a ratio of altitude divided by Lorey's Height tightens this threshold for outperforming the LiDAR models to 4-4.5 times the site's Lorey's Height. Similar to flight altitude, Lorey's Height significantly explains the variation in ΔR^2 (Table 1.2). The linear mixed-effects model indicates that for every Lorey's Height that acquisition altitude increases there is an ~8% improvement in ΔR^2, indicating that at four times Lorey's Height UAS SfM modeling of AGB typically exceeds the performance of aerial LiDAR models in ponderosa pine dominated systems (Figure 1.6).

1.3.3 Standard + NGRR AGB Model Performance

Integration of Standard + NGRR UAS SfM parameters for AGB modeling provided a 6.0% average increase in ΔR^2 across all flights compared to the modeling only using the Standard SfM parameters (Figure 1.5). This increase was found to be significant (p-value = 0.0181) when tested with a paired Wilcoxon signed rank test. Although there was not a significant difference (p-value = 0.5453) in the ΔMAE, the Standard + NGRR models did significantly (p-value = 0.0284) decrease ΔRMSE by 6.5% compared to models only using the Standard SfM parameters. Linear mixed-effects model coefficients for the Standard + NGRR SfM models revealed no significant differences compared to the Standard SfM linear mixed-effects models.

1.3.4 AGB Model Variable Importance

For the Standard SfM models of AGB the five most important variables fluctuated across models, but seven variables stood out from the rest and showed up in at least 40% of these models (Figure 1.7A). Across all flight altitudes and sites, the average height of points above

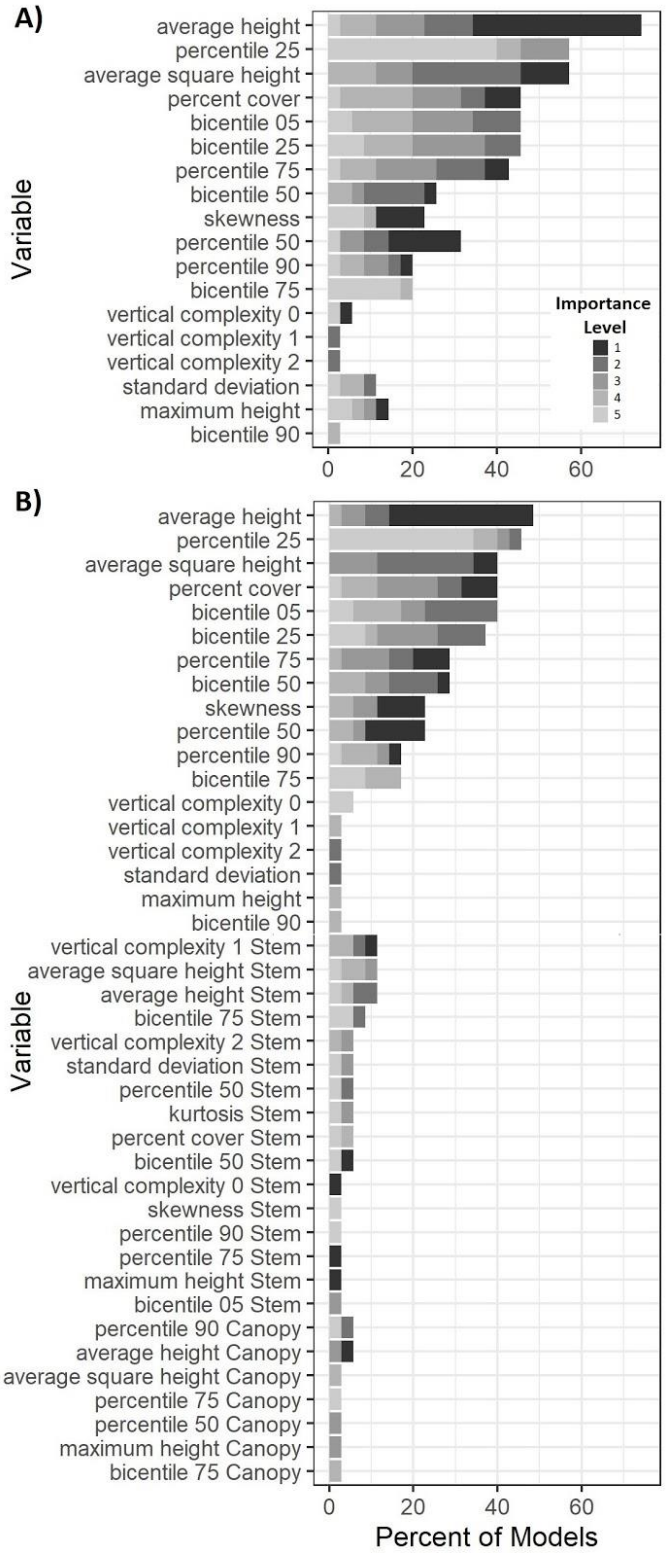

Figure 1.7. Random forest variable importance for Standard (A) and Standard + NGRR (B), values are sorted based on the percentage of the 37 models they appeared in for each grouping.

ground showed up in 74% of all models (or 27 of 37 models) and was the highest ranked variable in nearly 40%. The remaining six variables that were highly selected varied in being in 43 to 57% of models, with their importance metrics level fluctuating. These seven metrics accounted for 73.7% of all metrics selected in the Standard SfM models.

The top seven variables from the Standard metrics did not change even after including the NGRR segmented point cloud metrics (Figure 1.7B). However, these seven metrics only accounted for 56% of all selected metrics when the Standard and NGRR metrics were considered. This reduction was due to 17.8 and 4.9% of all selected variables being chosen from the Stem and Canopy distributional metrics, respectively. Of these NGRR metrics, only Stem average height, average squared height, and vertical complexity 1 were important in more than 10% of models (Figure 1.7B). Additionally, none of the Canopy distributional metrics occurred in more than 2 of the 37 models.

1.4 Discussion

1.4.1 AGB Model Performance

This study evaluated the impact of flight altitude and speed on UAS SfM plot-based modeling of aboveground biomass, with UAS modeling outperforming LiDAR at higher altitudes. Across all sites, UAS acquisitions above 80 m AGL resulted in improved model performance compared to aerial LiDAR; above this altitude relative to LiDAR models R^2 increased on average by 7.4% and RMSE and MAE were decreased by 8.8 and 10.9%, respectively (Figure 1.5). While the authors could not identify other studies that have seen this relationship for UAS biomass modeling, inference might be drawn from studies looking at relationships between UAS SfM reconstruction quality and flight altitude. Fraser and Congalton (2018) tested the effect of flight

altitude on image alignment and found that flying at their highest tested altitude provided the best results. Other studies have not directly seen an influence of altitude on SfM vegetation reconstruction, but still concluded that flying higher provided the benefit of greater acquisition extents (Torres-Sanchez et al., 2015). This literature connects the small decrease in image resolution at higher altitudes with improved imaging matching by reducing the influence of vegetation movement in the wind (Iglhaut et al., 2019). There is reason to believe this improved image matching better represents vegetation vertical distributions and improves AGB modeling at the plot-level. However, there is reason to believe that continued increasing of flight altitude and decreasing of image resolution will at some point result in decreased performance in modeling forest attributes like AGB.

While generally flying higher provided better model results, flying at altitudes too close to vegetation posed significant problems. Photogrammetric reconstruction of treetops was incomplete for the lowest altitudes tested at each site due to the proximity of the onboard UAS camera to the treetops. Failure to reconstruct the tops of trees led to inaccurate point cloud distributional metrics and resulted in poor AGB biomass model performance in our study (Figure 1.8). This truncation at the top of the point cloud can be seen in Figure 1.8, where the worse models represent low altitude flights that failed to reconstruct the tops of trees. The dependency of reconstruction on altitude is attributed to the proximity of treetops to the sensor, when the vegetation is too close, there is not sufficient photo overlap at the top of the tree compared to the programmed 90% forward and 90% side overlaps at the ground surface. While it varied across sites, consistent point cloud generation was achieved for all flights above 65 m altitude or ~1.9 times the maximum tree height within a given site. While lower altitude

UAS acquisitions can provide greater resolution, studies that require close proximity acquisition of forest canopies should consider increasing the photo overlap to compensate for the depth of vegetation. Therefore, as the height of vegetation increases, the flight altitude needed to reconstruct forest canopies should increase as well.

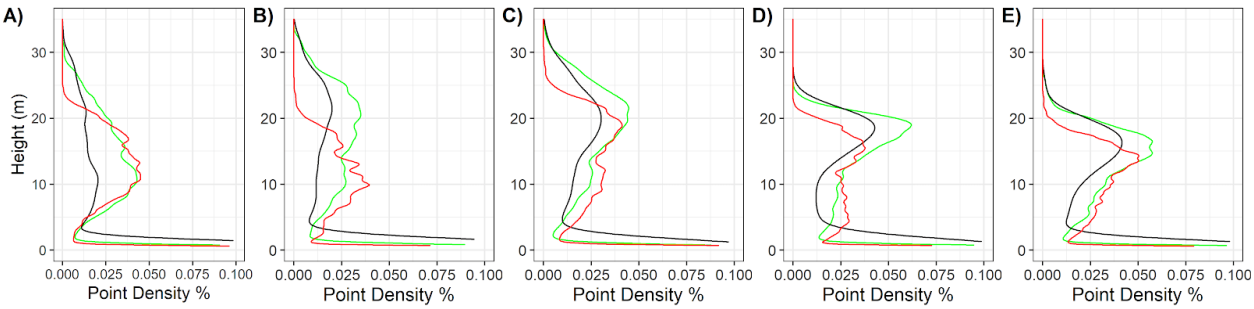

Figure 1.8. Relative point density as a function of height above ground for the best and worst Standard SfM AGB models (green and red respectively) at each site (from left to right KNF1, KNF2, KNF3, MEF1, and MEF2), with LiDAR point cloud distributions displayed in black.

Standardizing altitude as a ratio of Lorey's Height for each flight provided better consistency for interpreting the relationship between UAS flight altitude and vegetation height. All flights above four times a site's Lorey's Height resulted in improved model performance, with an average increase of 7.8% for R^2 and decreases of 9.3 and 11.6% for RMSE and MAE, respectively (Figure 1.5). Currently, it is difficult to evaluate the effects of altitude in different vegetation types, as it has not become common practice to report vegetation height or its relationship to flight altitude. Standardization of this is necessary within the UAS literature to improve cross-study synthesis of results. While flying above four times a site's Lorey's Height promotes improved AGB modeling within these forest systems, understanding the transference of this to forest systems that can reach dominant tree heights in excess of 40 m need investigation. Such work within the United States will need to address FAA regulations limiting UAVs to 120 m AGL flight altitudes.

Our results did not find a statistically significant effect of flight speed on resultant AGB models (Table 1.2), which could be attributed to the narrow range of relatively slow flight speeds (2-4 m sec^{-1}) evaluated. These findings differ from O'Connor et al. (2017), which found that increased flight speed causes image blurring, location errors, and, therefore, increased image alignment errors. While there is reason to believe this should propagate through to the modeling of forest attributes like AGB, it does not appear the moderate increases in flight speed tested in this study detrimentally impacted UAS SfM plot-based biomass modeling. Although not significant in this study, flight speed should remain an important consideration in planning UAS-based forest remote sensing. The effects of flight speed on modeling forest attributes like AGB need to be evaluated across a wider range of speeds and cross compared between sensor (rolling vs global shutter) and UAS platform types (multi-rotor vs fixed-wing; Zarco-Tejada et al., 2014).

Inclusion of the NGRR point cloud distribution metrics significantly improved the prediction of AGB in terms of variance explained (ΔR^2) and precision (ΔRMSE) over the Standard point cloud predictions. When NGRR metrics were included, they accounted for ~23% of important random forest predictors, with ~18% of them coming from the Stem point cloud metrics. The improved model performance, despite using only RGB spectral information, suggests that spectral segmentation of photogrammetric point clouds may be a powerful tool for improving models of forest structural attributes. Our results are shared by other studies, which found that including spectral indices from image orthomosaics as predictors of forest structure and biomass significantly improved model performance (Domingo et al., 2019). There is reason to believe more advanced segmentation and characterization of SfM points beyond

indices available from RGB imagery could further improve the modeling of forest biomass done in this study. The inclusion of a greater range of spectral data from more powerful multispectral sensors may contribute to better discernment between vegetation structural components within SfM point clouds.

1.4.2 Implications for Forest Management

Increasingly UAS are being utilized for characterizing forest structure across many ecosystems and forest management objectives (Kattenborn et al., 2014; Goldbergs et al., 2018; Navarro et al., 2020). Such UAS approaches can provide data at previously unachievable temporal and spatial resolutions with relatively low operational costs compared to similar datasets from aerial LiDAR. In order to transition UAS SfM forest structure monitoring from the research realm to a management tool, standardization of flight parameter reporting is critical. Without common reporting standards, synthesis and advancements in UAS research will be limited. This study highlights the potential of UAS SfM plot-based AGB modeling and the implications of flight altitude and speed while stating the importance of reporting altitude and vegetation height for improved data interpretation.

Strong trends across all flights were found between altitude and data collection time, data processing time, and data density, all of which are important in UAS flight planning for forest mapping (Figure 1.9). Wider image footprints at higher altitudes provide more efficient flight times (~2 min ha^{-1}), while there was a fivefold increase in flight times at the lowest altitude. Similarly, there are fewer images required at higher altitudes, resulting in SfM point cloud generation times varying from 10-60 min ha^{-1} moving from the highest to lowest altitudes. Conversely, the benefits of higher flight altitude on data collection and processing

time reverse, resulting in much lower point densities at the highest altitudes (~1,000 points m^{-2}) compared to lower altitudes (~7,000 points m^{-2}). While this is a strong gradient in data density, the highest altitude flights still provide greater than 50 times the point density of what is considered high quality aerial LiDAR data (Nelson, 2013). These results point to relatively rapid and reliable plot-based AGB modeling from UAS SfM at altitudes above four times a site's Lorey's Height. Additionally, moderate increases in UAS flight speed would amplify these benefits without detrimentally impacting model performance (Table 1.2).

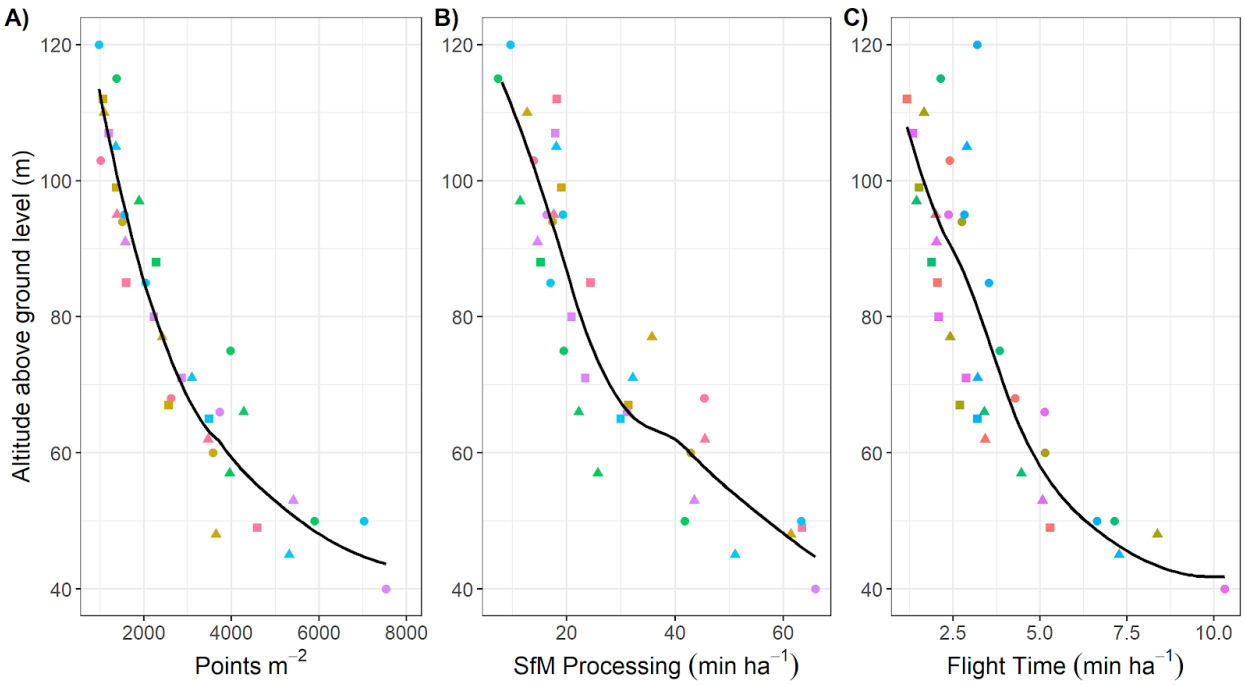

Figure 1.9. Evaluation of the effect of flight altitude above ground level on (**A**) filtered Standard SfM point cloud density, (**B**) SfM processing time in minutes ha^{-1}, and (**C**) flight time in minutes ha^{-1}, with black lines depicting Loess curves to represent data trend.

The plot-based UAS modeling strategy used in this study appears to be effective at describing forest attributes that lend themselves to imputation methods, with the aerial LiDAR literature indicated it should lend itself to describing forest biomass, basal area, and volume. While this strategy was successful at describing plot and therefore stand-level AGB, further

exploration is needed to understand the potential of UAS to characterize things at both tree and landscape scales. The ultra-high resolution of UAS data products and potential to fuse spectral and structural characteristics should enable improved individual tree observations. Early testing of single tree extraction methods from UAS SfM data has successfully identified >90% of trees (Silva et al., 2016). Characterization of individual trees with such high reliability will enable modeling of future stand conditions. Additionally, UAS have the potential to serve as a sampling tool themselves, vastly increasing the amount of data available for training courser landscape-scale satellite-based models of forest biomass. Recent research has demonstrated techniques for scaling UAS observations to describe biomass at greater extents than the UAS was capable of characterizing (Navarro et al., 2019).

1.5 Conclusion

This study demonstrates the high potential of plot-based UAS photogrammetry for modeling ponderosa pine aboveground biomass. When flying at altitudes of more than four times a forest's Lorey's Height, UAS SfM biomass modeling resulted in a 7.8% improvement in R^2 over aerial LiDAR. Additionally, segmenting the SfM point cloud based on the image spectral signature tied to individual points to look at Stem and Canopy distributions provided further substantial improvements to the AGB modeling. Beyond improved model performance, higher altitude UAS flights provide more efficient image acquisition and photogrammetry processing times of ~12 mins ha^{-1} as opposed to >70 min ha^{-1} at the lowest tested altitudes. This study highlights the role of UAS acquisition parameters on plot-based forest biomass modeling, while also showing the strong potential for UAS-based forest monitoring at increased temporal

frequencies than have been feasible from aerial LiDAR. Further work is needed to understand how such acquisition parameters might influence UAS-based single tree monitoring.

Cited Works

Anderegg, W.R., Hicke, J.A., Fisher, R.A., Allen, C.D., Aukema, J., Bentz, B., Hood, S. Lichstein, J.W., Macalady, A.K., McDowell, N., Pan, Y., Raffa, K., Sala, A., Shaw, J.D., Stephenson, N.L., Tague, C., and Zeppel, M. 2015. Tree mortality from drought, insects, and their interactions in a changing climate. New Phytologist, 208(3): 674-683, doi: 10.1111/nph.13477.

Bates, D., Maechler, M., Bolker, B., and Walker, S. 2015. Fitting Linear Mixed-Effects Models Using lme4. Journal of Statistical Software, 67(1): 1-48, doi: 10.18637/jss.v067.i01.

Bouvier, M., Durriey, S., Fournier, R.A., and Renaud, J.P. 2015. Generalizing Predictive Models of Forest Inventory Attributes Using an Area-Based Approach with Airborne LiDAR Data. Remote Sensing of Environment, 156: 322–334., doi: 10.1016/j.rse.2014.10.004.

Boyden, S., Binkley, D., and Shepherd, W. 2005. Spatial and temporal patterns in structure, regeneration, and mortality of an old-growth ponderosa pine forest in the Colorado Front Range. Forest Ecology and Management, 219(1): 43-55.

Breiman, L. 2001. Random forests. Machine Learning, 45: 5-32.

Briggs, J.S., Fornwalt, P.J., and Feinstein, J.A. 2017. Short-term ecological consequences of collaborative restoration treatments in ponderosa pine forests of Colorado. Forest Ecology and Management, 395: 69-80, doi: 10.1016/j.foreco.2017.03.008.

Dandois, J.P., Olano, M., and Ellis, E.C. 2015. Optimal altitude, overlap, and weather conditions for computer vision UAV estimates of forest structure. Remote Sensing, 7(10): 13895-13920, doi: 10.3390/rs71013895.

Dixon, G.E. 2002. Essential FVS: A user's guide to the Forest Vegetation Simulator. USDA Forest Service, Internal Report, Forest Management Service Center, 204 p.

Domingo, D., Ørka, H.O., Næsset, E., Kachamba, D., and Gobakken, T. 2019. Effects of UAV Image Resolution, Camera Type, and Image Overlap on Accuracy of Biomass Predictions in a Tropical Woodland. Remote Sensing, 11(8): 948, doi: 10.3390/rs11080948.

Fraser, B.T., and Congalton, R.G. 2018. Issues in Unmanned Aerial Systems (UAS) Data Collection of Complex Forest Environments. Remote Sensing, 10: 908.

Frey, J., Kovach, K., Stemmler, S., and Koch, B. 2018. UAV Photogrammetry of Forests as a Vulnerable Process. A Sensitivity Analysis for a Structure from Motion RGB-Image Pipeline. Journal of Remote Sensing, 10(6): 912, doi: 10.3390/rs10060912.

Fritz, A., Kattenborn, T., and Koch, B. 2013. UAV-based photogrammetric point clouds-Tree stem mapping in open stands in comparison to terrestrial laser scanner point clouds. International Archive of Photogrammetry & Remote Sensing Spatial Information Science, 40: 141-146.

Goldbergs, G., et al. 2018. Efficiency of Individual Tree Detection Approaches Based on Light-Weight and Low-Cost UAS Imagery in Australian Savannas. Remote Sensing, 10(2): 161, doi: 10.3390/rs10020161.

Hernández-Santiago, J.L., Reyes-Palomeque, G., Castillo-Santiago, M.Á., George-Chacón, S.P., Huechancona-Ruiz, A.H., Tun-Dzul, F., Dondon-Rivera, D., and Dupuy, J.M. 2018. Effects of sample plot size and GPS location errors on aboveground biomass estimates from LiDAR in tropical dry forests. Remote Sensing, 10: 1586, doi: 10.3390/rs10101586.

Hummel, S., Hudak, A.T., Uebler, E.H., Falkowski, M.J., and Megown, K.A. 2011. A comparison of accuracy and cost of LiDAR versus stand exam data for landscape management on the Malheur National Forest. Journal of Forestry, 109(5): 267-273.

Hudak, A.T., Crookston, N.L., Evans, J.S., Falkowski, M.J., Smith, A.M., Gessler, P.E., and Morgan, P. 2006. Regression modeling and mapping of coniferous forest basal area and tree density from discrete-return lidar and multispectral satellite data. Canadian Journal of Remote Sensing, 32(2): 126-138, doi: 10.5589/m06-007.

Hudak, A.T., Evans, J.S., and Smith, A.M.S. 2009. LiDAR Utility for Natural Resource Managers. Remote Sensing, 1(4): 934–951, doi: 10.3390/rs1040934.

Iglhaut, J., Cabo, C., Puliti, S., Piermattei, L., O'Connor, J., and Rosette, J. 2019. Structure from motion photogrammetry in forestry: a review. Current Forestry Reports, 5: 155-168, doi: 10.1007/s40725-019-00094-3.

Jenkins, J.C., Chojnacky, D.C., Heath, L.S., and Birdsey, R.A. 2003. National-scale biomass estimators for United States tree species. Forest Science, 49(1): 12-35, doi: 10.1093/forestscience/49.1.12.

Keyser, C.E. and Dixon, G.E. 2008. Central Rockies (CR) Variant Overview – Forest Vegetation Simulator. Internal Rep. Fort Collins, CO: U. S. Department of Agriculture, Forest Service, Forest Management Service Center. 70 p.

Liaw, A. and Wiener, M. 2002. Classification and Regression by randomForest. R News 2(3), 18--22.

Lutz, J.A. 2015. The evolution of long-term data for forestry: large temperate research plots in an era of global change. Northwest Science, 89(3): 255-269.

Mitchell, A.L., Rosenqvist, A., and Mora, B. 2017. Current remote sensing approaches to monitoring forest degradation in support of countries measurement, reporting and verification (MRV) system for REDD+. Carbon Balance and Management, 12(9): 1-22.

Murphy, M.A., Evans, J.S., and Storfer, A.S. 2010. Quantify Bufo boreas connectivity in Yellowstone National Park with landscape genetics. Ecology, 91: 252-261.

Navarro, J.A., Algeet, N., Fernández-Landa, A., Esteban, J., Rodriguez-Noriega, and Guillén-Climent, M. 2019. Integration of UAV, Sentinel-1, and Sentinel-2 Data for Mangrove Plantation Aboveground Biomass Monitoring in Senegal. Remote Sensing, 11(1): 77, doi: 10.3390/rs11010077.

Navarro, J.A., Young, M., Allan, B., Carnell, P., Macreadie, P., and Ierodiaconou, D. 2020. The application of Unmanned Aerial Vehicles (UAVs) to estimate above-ground biomass of mangrove ecosystems. Remote Sensing of Environment, 242: 111747, doi: 10.1016/j.rse.2020.111747.

Nelson, R. 2014. How did we get here? An early history of forestry lidar. Canadian Journal of Remote Sensing, 39: S6-S17, doi: 10.5589/m13-011.

O'Connor J., Smith, M.J., and James, M.R. 2017. Cameras and setting for aerial surveys in the geosciences: optimising image data. Progress in Physical Geography: Earth and Environment, 41(3): 325-344, doi: 10.1177/0309133317703092.

Pan, Y., Birdsey, R.A., Phillips, O.L., and Jackson, R.B. 2013. The Structure, Distribution, and Biomass of the Worlds Forests. Annual Review of Ecology, Evolution, and Systematics, 44(1), 593-622, doi: 10.1146/annurev-ecolsys-110512-135914

R Core Team. 2019. R: A language and environment for statistical computing. R Foundation for Statistical Computing, Vienna, Austria.

Roussel, J.R. and Auty, D. 2019. lidR: Airborne LiDAR Data Manipulation and Visualization for Forestry Applications. R package version 2.0.2.

Seifert, E., Seifert, S., Vogt, H., Drew, D., Aardt, J. V., Kunneke, A., and Seifert, T. 2019. Influence of Drone Altitude, Image Overlap, and Optical Sensor Resolution on Multi-View Reconstruction of Forest Images. Remote Sensing, 11(10): 1252, doi: 10.3390/rs11101252

Silva, Carlos A., et al. 2016. Imputation of individual longleaf pine (Pinus palustris Mill.) tree attributes from field and LiDAR data. Canadian Journal of Remote Sensing, 42(5): 554-573, doi: 10.1080/07038992.2016.1196852.

Thiel, C. and Schmullius, C. 2016. Comparison of UAV Photograph-Based and Airborne Lidar-Based Point Clouds over Forest from a Forestry Application Perspective. International Journal of Remote Sensing, 38(8-10): 2411-2426, doi:10.1080/01431161.2016.1225181.

Tinkham, W.T., Smith, A.M.S., Affleck, D.L.R., Saralecos, J.D., Falkowski, M.J., Hoffman, C.M., Hudak, A.T., and Wulder, M.A. 2016. Development of height-volume relationships in second growth Abies grandis for use with aerial LiDAR. Canadian Journal of Remote Sensing, 42(5): 400-410, doi: 10.1080/07038992.2016.1232587.

Torresan, C., Berton, A., Carotenuto, F., Gennaro, S.F.D., Gioli, B., Matese, A., … Wallace, L. 2016. Forestry applications of UAVs in Europe: a review. International Journal of Remote Sensing, 38(8-10), 2427-2447, doi: 10.1080/01431161.2016.1252477

Torres-Sánchez, J., López-Granados, F., Serrano, N., Arquero, O., and Peña, J.M. 2015. High-Throughput 3-D Monitoring of Agricultural-Tree Plantations with Unmanned Aerial Vehicle (UAV) Technology. PLoS ONE, 10(6): e0130479.

Vogeler, J.C., Yang, Z., and Cohen, W.B. 2016. Mapping post-fire habitat characteristics through the fusion of remote sensing tools. Remote Sensing of Environment, 173: 294-303, doi: 10.1016/j.rse.2015.08.011

Wallace, L., Lucieer, A., Malenovský, Z., Turner, D., and Vopěnka, P. 2016. Assessment of Forest Structure Using Two UAV Techniques: A Comparison of Airborne Laser Scanning and Structure from Motion (SfM) Point Clouds. Forests, 7: 62.

Webster, C., Westoby, M., Rutter, N., and Jonas, T. 2018. Three-dimensional thermal characterization of forest canopies using UAV photogrammetry. Remote Sensing of Environment, 209: 835-847, doi: 10.1016/j.rse.2017.09.033

Zarco-Tejada, P., Diaz-Varela, R., Angileri, V., and Loudjani, P. 2014. Tree height quantification using very high resolution imagery acquired from an unmanned aerial vehicle (UAV) and automatic 3D photo-reconstruction methods. European Journal of Agronomy, 55: 89-99.

Chapter 2: POTENTIAL FOR INDIVIDUAL TREE MONITORING IN PONDEROSA PINE-DOMINATED FORESTS USING UNMANNED AERIAL SYSTEM STRUCTURE FROM MOTION POINT CLOUDS

2.1 Introduction

Since the early 2000s, ecological management of dry lower-montane forest systems have increasingly focused on the variability and spatial arrangement of horizontal and vertical forest structure (Lydersen et al., 2013). This emphasis has grown alongside the body of literature supporting connections between forest resilience to disturbance and the level of variation in forest structure (Churchill and Larson, 2013). Silvicultural systems focused on altering forest spatial arrangement and variation can have impacts on overstory vertical complexity, microsite diversity, and future disturbance dynamics (Ziegler et al., 2017; Ma et al., 2010). Management prescriptions that intend to enhance vertical structural complexity are often restoration-focused, in order to bring ponderosa pine systems back to the historic range of variability and increase resilience (Dickinson et al., 2016). The creation of appropriate gaps and variable size tree groupings has a direct effect on where seedlings establish and competition-based tree mortality (Lydersen et al., 2013). Standing dead trees can then become important nesting habitat or influence shaded microclimates needed for understory plants or young trees. The need to enhance forest structural diversity has led many land managers to emphasize treatment strategies that enhance variation in forest structure (Churchill and Larson, 2013; Tinkham et al., 2017). Although managers have shown a desire to implement spatially informed silvicultural prescriptions that create variability, most monitoring tools available to them were not developed with spatial or heterogeneity management objectives in mind.

Fixed and variable radius plots have historically been the precedent for quantifying forest structure, however they assume forest homogeneity by focusing on average conditions of the forest (Dickinson et al., 2016). Small distributed plots (i.e., ≤ 1/10th acre) have been effective in the past at informing land managers of stand-level averages. However, such plots are limited in spatial extent and often use data collection protocols not designed for characterizing tree groups and opening arrangements that are critical in contemporary restoration approaches (Lutz, 2015). As a result, plot networks do not capture the spatial variability of forest structure necessary to meet changing restoration needs. Additionally, the relatively high expense of field data collection limits the temporal resolution of monitoring and treatment.

Land managers are increasingly requiring novel methods of data collection in response to the need for monitoring of forest spatial variability (Dickinson et al., 2016). Such methods are being called upon to provide comprehensive and accurate vertical forest structure data that can capture both inter-tree relationships, variations in groups, and stand-level dynamics. At the same time, research has consistently shown a need to observe forest structure at a spatial scale one step larger than the phenomenon being studied (i.e., clumps of trees and openings; Lutz, 2015). This combined need for higher resolution and complete coverage of management projects creates a unique methodological challenge. Exploration with a range of remote sensing strategies has shown hope for characterizing variation in horizontal forest structure with adequate resolution through both image spectral classification (Dickenson et al., 2016) and active sensor modeling (i.e., Light Detection and Ranging [LiDAR]; Zhen et al., 2016).

Image classification can characterize variation in metrics like canopy cover, it struggles to represent tree spatial patterns and metrics of vertical forest structure. With the advent of aerial LiDAR, forest managers found an inventory method of wall-to-wall coverage capable of capturing vertical heterogeneity in forests (Wulder et al., 2012). Although LiDAR can provide accurate estimates of forest structure, its cost limits repeat acquisitions for stand-level monitoring (Hummel, 2011). Additionally, although attempts to capture fine-scale tree-to-tree interactions have been successful through LiDAR individual tree detection (ITD) methods (Mielcarek et al., 2018), these techniques have been shown to represent dominant overstory trees most reliably. Beyond the tree locations and heights provided by ITD methods, various crown growing methods can characterize crown area using a set of rules on a pixel-by-pixel basis where locations of ITD detected trees are often used as starting "seeds". Most literature on ITD methods points to LiDAR's limited point density of 10 - 30 points m^{-2} as causing omission or underrepresentation in smaller size classes of trees (Li et al., 2012). While Canopy Height Models (CHMs) derived from aerial LiDAR typically range from 0.5 - 1 m resolution, the average spacing between LiDAR points can be as high as 0.62 m (Popescu et al., 2007). The relatively high resolution of LiDAR-derived CHM compared to the actual spacing between laser points can be attributed to the smoothing of data with a moving window that creates the appearance of a higher resolution than LiDAR allows. The high cost of LiDAR for individual management projects and its limited success in describing variation in smaller tree size classes has again drawn attention towards other methods of monitoring forest horizontal and vertical arrangement at fine spatio-temporal scales.

Unmanned aerial systems (UAS) have emerged as a lower-cost alternative to aerial LiDAR for local wall-to-wall horizontal and vertical forest structure characterization (Fraser & Congalton, 2018). Most commonly, UAS are deployed with standard RGB cameras, which allow for three-dimensional forest reconstruction through the application of Structure from Motion (SfM) photogrammetry algorithms (Torresan et al., 2017). The miniaturization of advanced imaging sensors and GPS technologies are facilitating low cost (i.e., < $2,000) UAS platforms for natural resource monitoring (Torresan et al., 2017; Maturbong et al., 2019; Mlambo et al., 2017). Because of the low financial barrier to UAS platforms capable of accurately characterizing vertical forest structure, land managers are exploring new approaches that improve temporal resolution in forest monitoring (Westoby et al., 2012). Additionally, UAS SfM photogrammetry can provide data density well in excess of 1,000 points m^{-2}, possibly enabling adaptation of LiDAR ITD methods for characterizing all tree size classes. Successful ITD across all tree size classes from UAS's higher data density could enable accurate spatial characterization of individual trees within different canopy strata and lead to better representations of local forest neighborhoods and heterogeneity (Dickinson et al., 2016). Moving window ITD methods may be effective in ponderosa-dominated ecosystems due to the specie's shade intolerance leading to large inter-tree separation distance (Balsi et al., 2018).

Many studies have cross-examined ITD methods for LiDAR-derived CHM, with an accuracy of 40-90% depending upon the forest type and structure (Belmonte et al., 2019; Heurich et al., 2008; Maturbong et al., 2019; Persson et al., 2002; Yu et al., 2011). Despite the variety of ITD methods, most use a fixed moving window to detect the local maxima of a CHM, which are then identified as trees (Popescu and Wynne, 2004). As of yet, the literature applying

ITD methods to SfM-derived CHM has been nominally investigated, with limited cross-comparison of these methods on higher data density UAS SfM-derived CHMs. Additionally, there has been little emphasis on comparison of crown growing methods on UAS-derived CHMs. However, there is reason to think the accurate fine-scale vertical forest structure provided by UAS SfM point clouds may translate to a higher resolution CHM better suited for moving window ITD methods and crown growing methods.

High resolution UAS-derived CHMs have not been comprehensively evaluated to understand how a trees position within the forest canopy impacts individual tree detection. The existing literature, especially as it pertains to LiDAR, usually narrows the focus to include only overstory canopy due to the inherent difficulty of detecting trees with narrower, partially-occluded crowns lower in the canopy (Heurich et al., 2008; Panagioditis et al., 2017). In addition, the use of small plots of trees and consumer-grade GPS technology for ITD validation in most studies results in a small sample of real trees, representing limited variation in forest structure, and the inability to perform true individual tree-level matching. In the past there have been calls for using large (>1 ha) stem-mapped sites for training and validation of remotely sensed aboveground biomass (Chava et al., 2019), however, we content that such stem-mapped sites are ideal for validation in a range of remote sensing application. The use of large, maintained stem-map plots may allow for a more accurate estimate of ITD methods across continuous observations of forest structure.

This study will utilize high-resolution, fine-scale UAS SfM point clouds and large continuous forest stem-maps of ponderosa pine (*Pinus ponderosa* Lawson & C. Lawson) dominated forests (1) to examine the accuracy of individual tree detection methods, and

subsequent crown growing algorithms and (2) determine the effect of tree size and local forest structure on an individual tree's probability of detection.

2.2 Methods

2.2.1 Study Area & Validation Data

Two study regions of ponderosa pine dominated forest were used to investigate the influence of forest structure on UAS tree detection. The Lookout Canyon forest dynamics site on the Kaibab National Forest in Arizona sits at an elevation of approximately 2,400 m on the Kaibab plateau, hereafter called KNF (Figure 2.1). The site is comprised of two adjacent 4-ha treatments, including one control and one thinned in 1993 to 13.8 m^2 ha^{-1} of basal area. Utilizing an existing grid of survey points, in May 2019 the sites were stem mapped, with observations of location, height, and diameter at breast height (DBH) for all trees > 1.37 m tall.

The N1 forest dynamics site at the Manitou Experimental Forest on the Pike-San Isabel National Forest in Colorado is a square 9.3-ha site that was initially stem-mapped in 1974, hereafter called MEF. The site is dominated by ponderosa pine with very minor components of Douglas-fir (*Pseudotsuga menziesii* (Mirb.) Franco) and blue spruce (*Picea pungens* Engelm.), with a sparse, grassy understory and a minor shrub component. The average elevation of the plot is 2,500 m, with a slope of ~5% to the southeast. In August 2018 the established trees on the site were re-inventoried and ingrowth was measured and stem-mapped by recording distance and direction to two previously mapped trees.

Within each site a random subset of tree crown diameters was also sampled to assess the accuracy of different crown growing methods. At each site, six randomly selected locations were used to sample trees within 15 m. Two crown diameters were measured for each selected

tree in order to calculate the area of an ellipse, resulting in a total of 186 crowns: 97 at KNF and 89 at MEF.

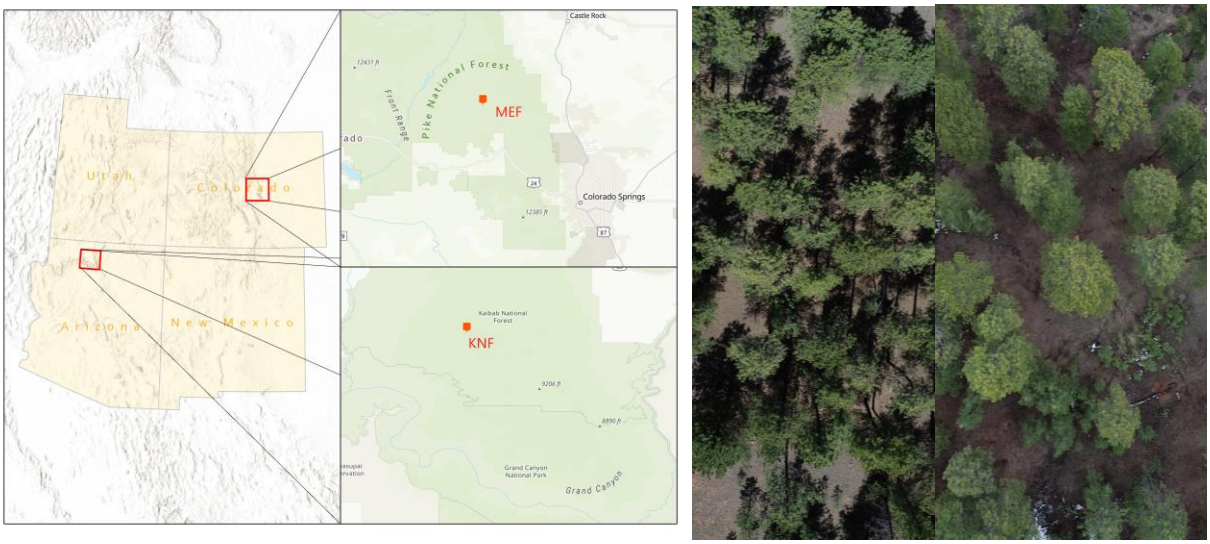

Figure 2.1. Relative locations (Left panel) and example forest structures captured by UAS at MEF (middle) and KNF (right).

2.2.2 UAS Data Collection & Processing

All images were collected with a DJI Phantom 4 Pro quadcopter (Dá-Jiang Innovations Science and Technology Co. Ltd., Shenzhen, China) equipped with a 20-megapixel RGB camera. The aircraft recorded geolocation (x, y, and z) and camera parameter values for each captured photo to a manufacturer-stated vertical accuracy of ±0.5 m and horizontal accuracy of ±1.5 m (https://www.dji.com/phantom-4-pro; accessed 18 March 2019). Pre-programmed flight paths with 90 m flight height, flight speed of 5 m s^{-1}, and side and forward image overlap of 90% were set for MEF, while KNF was flown at 100 m flight height, flight speed of 4 m s^{-1}, and side and forward image overlap of 90% using Altizure (Shenzhan, China) for IOS flight controller. Differences in flight parameterization among the two sites ensured a constant ratio of flight height to vegetation height, while also ensuring each acquisition could be completed with a

single battery. Additionally, Altizure provides control of camera settings (in case of lighting changes), which were set to adjust automatically. In order to comply with Part 107 Federal Aviation Administration regulations, the remote pilot in command and visual observer maintained a line of sight with the aircraft for the duration of the flight.

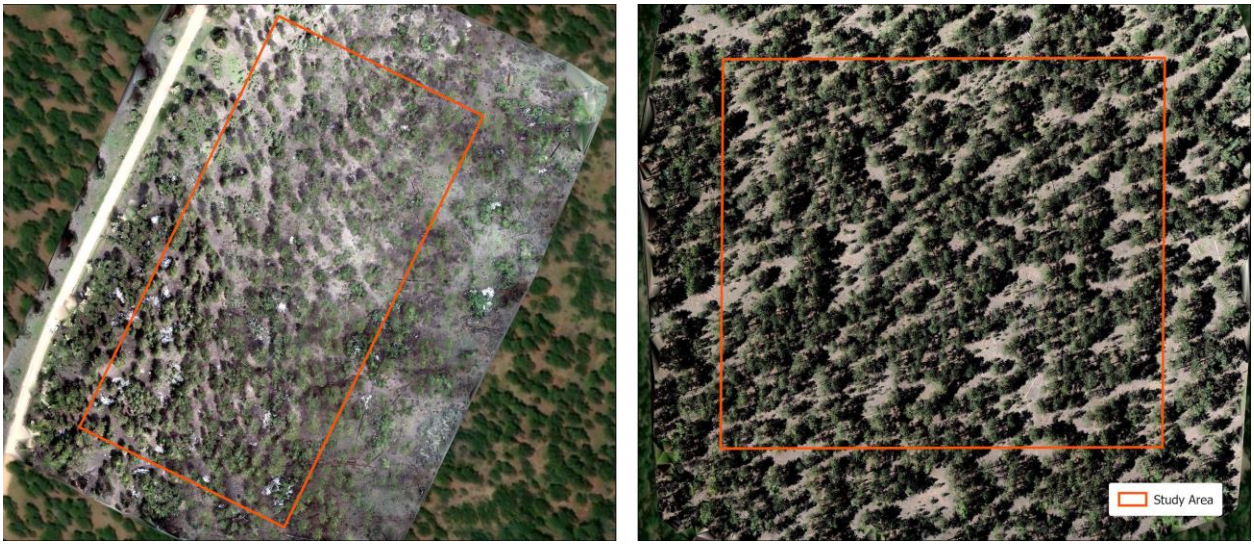

Figure 2.2. Final acquisition extent clipped to central area of interest at KNF (left) and MEF (right).

Point clouds were produced with Agisoft Metashape version 1.5.3 (www.agisoft.com; Agisoft LLC, St. Petersburg, Russia) through initial image feature identification, feature matching across photos, and location of images in 3D space using the 431 and 476 UAS images as inputs from KNF and MEF, respectively. Using CloudCompare version 2.10.1 (www.cloudcompare.org), a software for inspecting point data in 3-dimentional space, the UAS SfM point clouds were georeferenced to existing aerial LiDAR point clouds at each site using the "Fine Registration" tool. This process iteratively matched the ground points of the UAS SfM point cloud to the geolocated aerial LiDAR ground points. Optimal settings conformed to the processing parameters for photogrammetry forest reconstruction outlined in Fraser & Congalton (2018).

After the point clouds were filtered and normalized to themselves in LAStools version 1.2 (http://lastools.org), canopy height models (CHM) were produced at 0.25 m resolution in LAStools using "LAS2dem". The CHMs were clipped to the area of interest at each site, which were squares of varying dimensions whose area totaled 4.5-ha (Figure 2.2).

Table 2.1. Summary of individual tree detection and crown growing functions and parameters used in this study.

Method	R Package (Function); Citation	Variables
Individual Tree Detection		
Fixed Window	ForestTools package (vwf); Popescu and Wynne (2004)	Window Size (3x3, 5x5, 7x7 cells etc.)
Variable Window	ForestTools package (vwf); Popescu and Wynne (2004)	Window Size (Varies according to user defined function in response to height)
Crown Growing		
Silva2016(); voronoi tessellation	lidR package; treetops from best vwf() models; Silva et al., 2016	Lmf (local maxima filter) Mac_cr_factor (Maximum crown diameter given as a proportion of tree height)
Dalponte2016(); crown growing decision tree	lidR package; treetops from best vwf() models; Dalponte and Coomes, 2016	Lmf (local maxima filter) Th_tree (Minimum tree height threshold) Th_seed (growing threshold 1) Th_cr (growing threshold 2) Max_cr = 30 (maximum crown diameter)
watershed(); watershed segmentation	lidR package; treetops from best vwf() models; Romain, 2020	Lmf (local maxima filter) th_tree (threshold below which a pixel cannot be a tree)
mcws(); marker-controlled watershed segmentation	ForestTools package; treetops from best vwf() models; Plowright, 2018	minheight = 0.5 (minimum pixel value a crown can be) format = "polygon"

2.2.3 Individual Tree Detection

This study evaluates both fixed and variable window local-maxima functions as implemented in the ForestTools package (Plowright, 2018) of the R statistical programming language (R Core Team, 2019) for their potential to represent different forest canopy stratums and the overall forest structure. The fixed window function was tested at window sizes varying from 1 - 7 m in 1 m steps. The variable window function was tested using both linear (Equation

1) and exponential (Equation 2) functions that define the window radius as a function of height in the CHM.

$$WR = b_1 + Hb_2 \quad \text{[Equation 1]}$$

$$WR = b_1 \times e^{Hb_2} \quad \text{[Equation 2]}$$

Where WR is the window radius (m), H is the height value (m) in the CHM, and the coefficients b_1 and b_2 were tested across a range of values. In the linear model b_1 and b_2 were tested from 0.3 - 0.6 and 0.05 - 0.09, respectively. For the exponential model, b_1 and b_2 were tested from 0.4 - 0.9 and 0.01 - 0.09, respectively.

2.3.4 Accuracy of Tree Detection and Structure Parameters

Accuracy assessment of individual tree detection has typically been implemented through traditional inventory methods, visual inspection of remotely acquired imagery, and direct comparison of the total number of trees detected vs. the number of trees on the site. This verification is lacking because it does not allow us to examine where ITD methods might break down in relation to forest structure and tree type.

This study utilized 2,270 and 2,700 stem-mapped trees at the KNF and MEF sites to assess the accuracy of each ITD method. Using the methodology of tree matching outlined by Silva et al. (2016), detected trees were matched against stem-mapped trees by finding their nearest neighbor that falls within a range of the detected tree's height. In effect, there is a maximum Euclidean distance (MED) and minimum height difference (MHD) that must both be fulfilled for the two trees to be considered a match. It is an iterative process that buffers one tree at a time according to the MED before checking the MHD. If multiple trees are found within the buffer, the tree with the smallest MHD is considered a match to the detected tree.

Once a match is made, both the ITD extracted tree, and stem-map match are removed before the next iterative match is identified. MED was set to 3 m to account for stem-mapping errors, georeferencing errors, and tree lean. The MHD was set to 10% of the field inventoried height to account for observation errors in dense, mature forests (Andersen et al., 2006).

To understand extraction accuracy across tree sizes, the stem-mapped trees were classified into three classes of Overstory (> 18 m at MEF; > 20 m at KNF), Intermediate (heights between the upper and lower bounds), and Understory (< 6 m at MEF; < 8 m at KNF) based on their location within the distribution of heights at each study site. Trees were not distinguished between live and dead, due to less than 30 dead trees at each study site. Within each class and overall at each site, the correctly and incorrectly matched trees were summarized by calculating the true positive (TP, correct detection), false positive (FP, commission error), and false negative (FN, omission error) extraction rates. The accuracy of these measurements was summarized to recall (*r*; Equation 3), precision (*p*; Equation 4), and F-score (*F*; Equation 5) (Goutte and Gaussier, 2005; Sokolova et al., 2006):

$$r = \frac{TP}{TP + FN} \quad \text{[Equation 3]}$$

$$p = \frac{TP}{TP + FP} \quad \text{[Equation 4]}$$

$$F = 2 * \frac{r * p}{r + p} \quad \text{[Equation 5]}$$

Recall is the rate of tree detection, precision is a measure of detected tree correctness, and F-score is the overall accuracy of the method, which incorporates both precision and recall. The values of *p*, *r*, and *F* will range from 0 to 1. If a particular ITD method has identified trees and done it correctly according to its values of *p* and *r*, a higher F-score will result. In a scenario given perfect segmentation, all values would be equal to 1. While the F-score is an important

tool for measuring success, looking at initial values of true and false positives, as well as false negatives, can help further illustrate the success of the given equation. For example, while one method may see a high raw number of true positives, it may be due to an over detection of trees. With trees classified by size, tree detection accuracy metrics can be examined not only at the overall stand level, but also be examined as they pertain to different tree size groups. The best performing ITD methods should perform well across size groups, as well as not over detect tree tops and produce artificially higher true positive numbers. Therefore, to establish the best performing equations for individual tree detection overall F-score was evaluated, and ties were broken through examining F-scores for the Overstory, Intermediate, and Understory strata. The best performing models overall were identified at both sites for exponential, linear, and fixed window sizes. Additionally, matched stem-mapped trees were compared to extracted heights to determine precision on a tree-tree basis. Errors were summarized using mean absolute error (MAE) and percentage root mean square error (%RMSE).

2.2.5 Probability of Tree Detection

To quantify the range of forest structures the best performing ITD method can represent, logistic regression was used to determine the probability of a tree's detection. Separate models were fit within each canopy stratum where the response was classified as 1 for correctly matched trees and as 0 for omitted trees. Individual measures of height and DBH were combined with local neighborhood structural attributes summarized for a 5 m radius circle surrounding each tree (Table 2.1) that included trees per hectare (TPH), basal area (m^2 ha^{-1}), height percentile (%) calculated as target tree height divided by tallest tree height in the neighborhood times 100, and nearest-neighbor distance (meters; NND). Parameters were

tested for collinearity using the Pearson's correlation coefficient and when exceeding 0.6 the parameter with weaker relation to the response was removed. The best subset of remaining variables was identified through stepwise forward-backward variable selection using the Akaike Information Criterion (AIC). The best model subset was the one that minimized AIC. Logistic regression was performed using the glm and regsubsets functions in the stats (R Core Team, 2019) and leaps (Lumley, 2020) packages of the R statistical programming language.

2.2.6 Crown Growing

The top-performing ITD method, as determined above by Overall F-score, was then used as input trees to several crown growing methods, most of which use detected treetops as "seeds'' to grow crowns using the rasterized CHM. All crown growing was run in the R statistical program (Table 2.1) using the Dalponte, Silva, and watershed functions from the lidR package (Romain, 2020), and the marker-controlled watershed function from the ForestTools package (Plowright, 2018). The Dalponte2016() function uses a decision tree to grow crowns using the ITD trees as seeds. Crowns are grown by iteratively adding surrounding cells as long as their height value is less than a defined maximum difference from the seeds height, less than a maximum crown ratio, or a maximum crown diameter is reached (Dalponte & Coomes, 2016). The Silva2016() function starts with a buffer around each ITD tree point, from which crowns are then separated through centroidal Voronoi tessellation (Silva et al., 2016). Values within a resulting tree crown less than a user-defined percentage of the tree's height are then removed from the crown region. Lastly, an inverted watershed segmentation method, as implemented in the watershed() function of the lidR package, was used to grow crowns using detected trees as seeds. The watershed() function can either use input tree locations using a "marker-controlled"

approach or find local maxima on its own. The mcws() function (marker-controlled watershed) from the ForestTools package was also run. The user-defined parameters within each function are summarized in Table 2.1 and set to the default except where noted. Extracted tree crown area was compared with matched stem-mapped tree crown area to determine precision on a tree-tree basis. Errors were summarized using MAE and %RMSE. Crown radius of a circle was also back calculated from field inventory and detected crown areas for further comparison.

Table 2.2. Summary of tree and neighborhood structural attributes at the two study sites. Numbers represent the mean (standard deviation) of individual tree parameters or from 5 m radius local plots.

Study Site	Stratum	Height (m)	DBH (cm)	Crown Area (m)	NND* (m)	Height Percentile (%)	Basal Area (m^2 ha^{-1})	TPH
KNF (N=2,270)	Overstory (n=446)	25.2 (3.5)	54.5 (12.6)	163.8 (81.4)	2.47 (1.25)	97 (6)	64.4 (30.3)	462 (345)
	Intermediate (n=820)	13.2 (3.3)	23.9 (8.9)	51.1 (39.1)	1.66 (1.04)	74 (21)	45.3 (27.5)	1,075 (747)
	Understory (n=1,004)	4.8 (1.6)	8.7 (4.2)	15.6 (8)	1.22 (0.99)	51 (28)	22.6 (20.2)	1,508 (1,163)
MEF (N=2,700)	Overstory (n=592)	20.6 (1.6)	40.7 (8.1)	99.0 (60.9)	2.50 (1.17)	97 (5)	43.9 (16.4)	527 (261)
	Intermediate (n=689)	11.9 (4.0)	22.6 (10.0)	58.6 (33.9)	1.87 (1.16)	76 (22)	30.4 (20.8)	852 (639)
	Understory (n=1,419)	3.0 (1.3)	4.4 (3.6)	15.5 (13.8)	1.44 (0.98)	39 (28)	12.8 (13.9)	1,293 (752)

* NND - nearest-neighbor distance

2.3 Results

2.3.1 Observed Forest Structure

Both study sites exhibit complex vertical and horizontal forest structure with high levels of variation in the individual tree and local neighborhood structural attributes (Table 2.2). Trees at KNF tended to be ~20% taller in each canopy stratum than those at MEF, with the KNF Overstory stratum having twice the variation within it. Across the site strata, the only

substantial differences in the relative height of a tree compared to its neighbors was that Understory trees at KNF tended to be taller in both relative and absolute terms than Understory trees at MEF. Despite having larger trees, KNF tended to have trees arranged closer to neighboring trees across all strata. KNF's height distribution appears unimodal and skewed to the right, typical of a multi-age or all-age forest structure (Figure 2.3). Conversely, the bimodal appearance of the MEF height distribution is more indicative of a two-age forest structure.

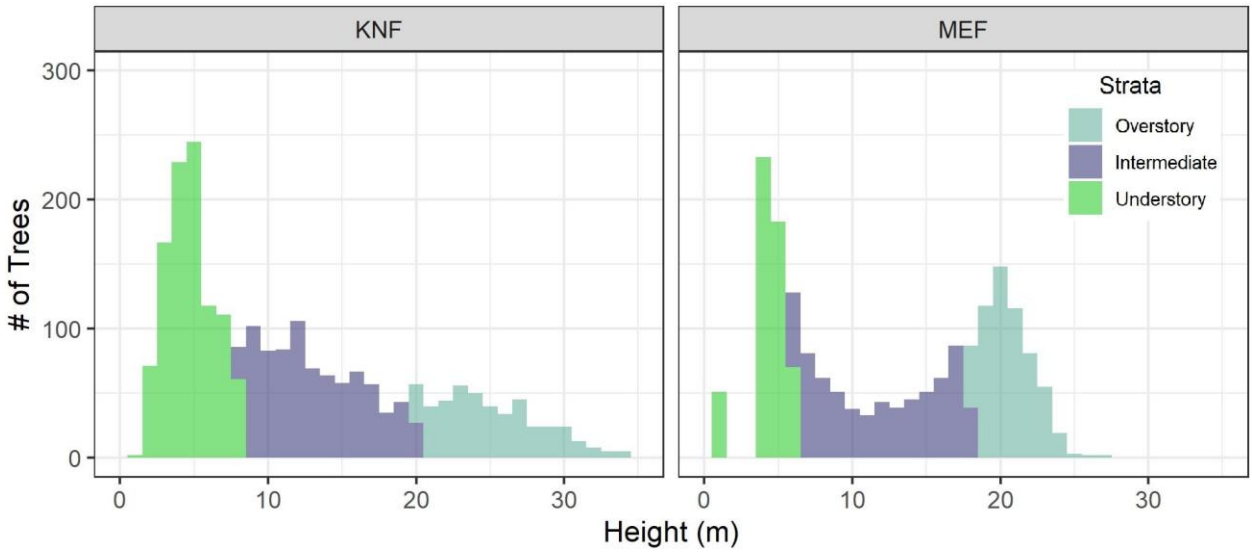

Figure 2.3. Histogram of observed tree heights at the two study sites colored by canopy stratum.

2.3.2 ITD Model Performance

Evaluation of the ITD process showed that linear models fit within the variable-window function produced the 12 and 7 highest ranked models in terms of maximizing overall F-score at MEF and KNF, respectively (Table 2.3). Additionally, similar overall performance was seen for each model form at the two respective sites, although the best model parameters varied slightly. At both sites, exponential models performed similarly to the linear models, except that exponential models tended to have lower detection rates in the Understory stratum.

Consistently, 1 m was the best fixed window size. However, this tended to have substantially worse F-scores than both the linear and exponential variable window functions (Table 2.3).

Table 2.3. Summary of best linear, exponential, and fixed-window ITD models for both Manitou Experimental Forest (MEF) and Kaibab National Forest (KNF).

Rank	Model	Stratum	# of True Trees	# of Detected Trees	Height Mean Error (m)	Height RMSE (m)	Height RMSE (%)	True Positive	False Negative	False Positive	Recall	Precision	F-score
Manitou Experimental Forest													
1	$WR = 0.4 + H \times 0.085$	Overall	2,700	1,854	0.10	0.62	11.8	0.49	0.51	0.20	0.49	0.71	0.58
		Overstory	592	630	0.45	0.75	3.7	0.77	0.23	0.29	0.77	0.72	0.75
		Intermediate	689	547	0.10	0.56	5.3	0.48	0.52	0.32	0.48	0.60	0.53
		Understory	1,419	677	-0.20	0.53	17.8	0.37	0.63	0.11	0.37	0.78	0.50
19	$WR = 0.5 \times e^{H \times 0.06}$	Overall	2,700	1,754	0.12	0.62	11.2	0.47	0.53	0.18	0.47	0.72	0.57
		Overstory	592	641	0.45	0.75	3.6	0.78	0.22	0.31	0.78	0.72	0.75
		Intermediate	689	542	0.12	0.56	5.2	0.47	0.53	0.32	0.47	0.60	0.52
		Understory	1,419	571	-0.20	0.52	17.4	0.34	0.66	0.07	0.34	0.84	0.48
70	$WR = 1$	Overall	2,700	2,121	0.13	0.64	9.6	0.45	0.55	0.34	0.45	0.57	0.50
		Overstory	592	1,011	0.33	0.75	3.7	0.86	0.14	0.85	0.86	0.50	0.64
		Intermediate	689	700	0.16	0.59	4.9	0.49	0.51	0.52	0.49	0.49	0.49
		Understory	1,419	410	-0.18	0.49	16.4	0.25	0.75	0.04	0.25	0.88	0.39
Kaibab National Forest													
1	$WR = 0.6 + H \times 0.065$	Overall	2,270	1,790	0.68	1.80	18.0	0.51	0.49	0.28	0.51	0.65	0.57
		Overstory	446	459	1.63	2.43	10.0	0.72	0.28	0.31	0.72	0.70	0.71
		Intermediate	820	460	0.83	1.91	15.0	0.45	0.56	0.12	0.45	0.79	0.57
		Understory	1,004	871	-0.08	1.07	23.5	0.47	0.53	0.39	0.47	0.55	0.51
11	$WR = 0.4 \times e^{H \times 0.06}$	Overall	2,270	1,667	0.70	1.81	17.3	0.49	0.51	0.24	0.49	0.67	0.57
		Overstory	446	454	1.62	2.42	10.0	0.71	0.29	0.31	0.71	0.70	0.70
		Intermediate	820	450	0.84	1.91	14.9	0.44	0.56	0.11	0.44	0.81	0.57
		Understory	1,004	763	-0.08	1.06	22.5	0.44	0.56	0.32	0.44	0.58	0.50
63	$WR = 1$	Overall	2,270	1,560	0.89	1.84	14.7	0.44	0.56	0.25	0.44	0.64	0.52
		Overstory	446	713	1.40	2.34	9.6	0.78	0.22	0.81	0.78	0.49	0.60
		Intermediate	820	420	1.18	1.89	14.1	0.43	0.57	0.09	0.43	0.83	0.56
		Understory	1,004	427	-0.03	0.87	19.4	0.30	0.70	0.13	0.30	0.70	0.42

The Overall number of extracted trees was 31.3 and 21.1% less than the stem-mapped number of trees for the MEF and KNF study sites, respectively (Table 2.3). However, extraction accuracy varied across the canopy strata. The total number of Overstory stratum trees extracted in the best models was over by 6.4, and 2.9% of the inventoried tree counts at MEF and KNF, respectively. The direction of this error shifts to an under extraction of 20.6 and 43.9% in the Intermediate stratum and 59.8 and 13.2% in the Understory stratum, respectively. Both the linear and exponential variable window functions provided similar mean height errors for

each of the canopy strata, with the Overall error being less than 0.70 m. This positive bias in extracted tree height tended to be 2 to 6 times larger at KNF than at MEF (Table 2.3). Height RMSE was 4-10% in the Overstory, increasing through the shorter canopy strata to 16-24% in the understory.

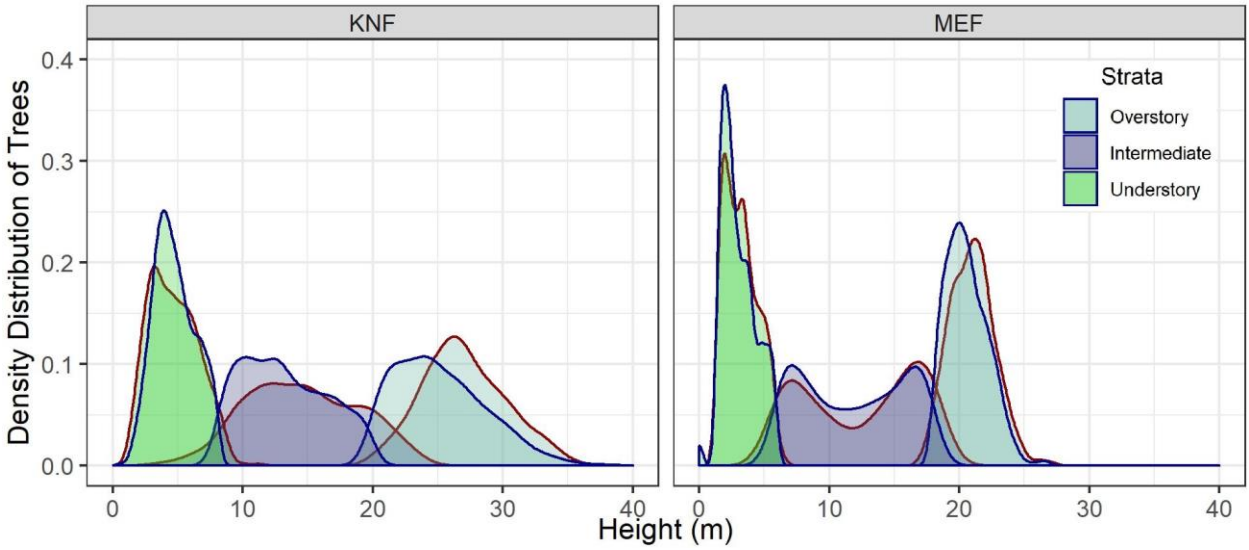

Figure 2.4. Density distributions of tree heights at the two study sites with field observed data outlined in blue, and the top-ranked individual tree detection model values outlined in red. Overlapping segments of the distributions appear darker.

2.3.3 Probability of Tree Detection

Visual comparison of height distributions for the stem-mapped trees and trees extracted with the best performing model follow similar trends (Figure 2.4). The largest departure in the distributions occurred at the KNF study site, with extracted tree heights tending to be shifted and slightly taller than field observed values. The two-sample Wilcoxon Rank Sum test was used to statistically validate the similarity of strata distributions of detected heights to observed heights for both sites. Despite the visual similarity of the distributions, only the extracted heights in the KNF Understory ($p = 0.9856$) and MEF Intermediate ($p = 0.3629$) strata were found not to depart from the observed height distributions. While the other stratum pairs

appeared visually similar, they were found to significantly differ at the $\alpha < 0.05$ level. A Kolmogorov-Smirnov test was also performed, and all strata combinations at both sites were found to differ significantly at the $\alpha < 0.05$ level.

Table 2.4. Best model subset from logistic regression to predict the probability of extracting a tree given local forest structure in a 5 m radius of a tree, broken out by canopy stratum.

Parameter	Coefficient	Std. Error	Z value	p-value
Overstory Stratum				
Intercept	-4.5404	1.2743	-3.563	<0.001
Height Percentile	0.0659	0.0127	5.170	<0.001
Basal Area (m^2 ha^{-1})	-0.0106	0.0029	-3.645	<0.001
Intermediate Stratum				
Intercept	-0.8171	0.5939	-1.376	0.1689
Height Percentile	0.0223	0.0069	3.215	0.0013
Basal Area (m^2 ha^{-1})	-0.0668	0.0148	-4.504	<0.001
Height Percentile:Basal Area (m^2 ha^{-1})	0.0005	0.0002	2.770	0.0056
Understory Stratum				
Intercept	-1.1015	0.1346	-8.186	<0.001
Height Percentile	0.0164	0.0018	9.323	<0.001
Basal Area (m^2 ha^{-1})	-0.0176	0.0033	-5.302	<0.001
Distance to Nearest-Neighbor (m)	0.1693	0.0407	4.161	<0.001

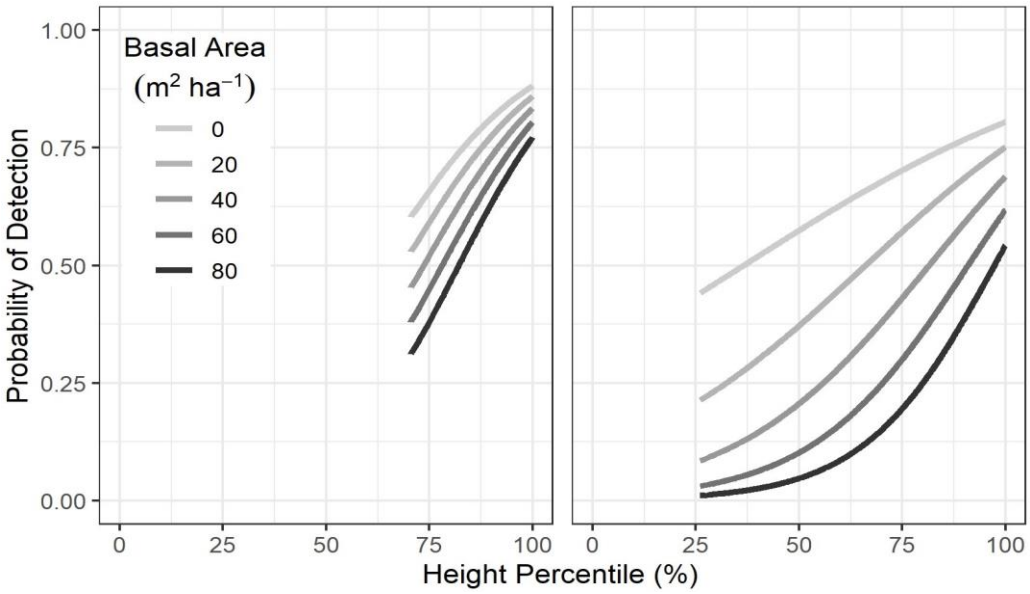

Figure 2.5. Probability of detecting (A) Overstory stratum trees and (B) Intermediate stratum trees, based on a tree's height compared to neighbors within 5 m and basal area per hectare estimated from a 5 m radius plot.

The significant variables controlling the probability of detecting individual trees varied across canopy strata (Table 2.4). However, across all strata trees that were relatively taller compared to their local neighbors (Height Percentile) had a greater probability of detection (Figures 2.5 and 2.6). In the Overstory and Intermediate stratums the probability of detection was negatively related to Basal Area per hectare, with Basal Area having a six times greater influence on Intermediate canopy stratum trees (Table 2.4). The effect of the Basal Area in the Intermediate stratum also interacted with Height Percentile, such that increasing stand density could reduce the probability of detection to 0% for trees less than half the height of a local neighbor (Figure 2.5).

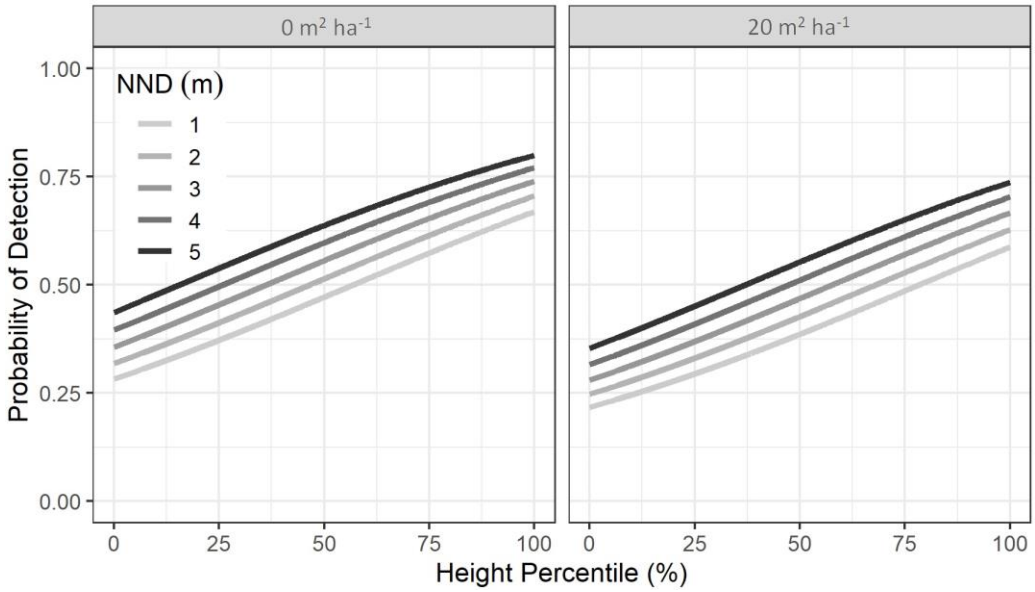

Figure 2.6. Probability of detecting Understory stratum trees based on a tree's height compared to neighbors within 5 m, nearest-neighbor distance (m; NND), and basal area per hectare estimated from a 5 m radius plot set to (A) 0 m^2 ha^{-1} and (B) 20 m^2 ha^{-1}.

Similar dynamics were seen in the Understory stratum (Figure 2.6), with the exception that increasing the distance to the nearest neighboring tree significantly increased the probability of detecting Understory trees (Table 2.4). For every meter of distance to the nearest

neighbor, there is an almost 4% increase in the probability of detecting an Understory tree, meaning open-grown trees have a significantly greater likelihood of being detected (Figure 2.6).

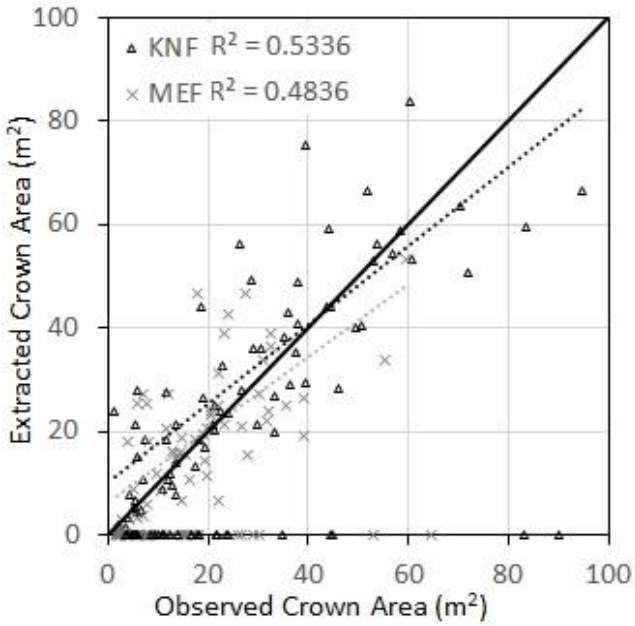

Figure 2.7. Observed versus lidR watershed extracted individual tree crown area. Dashed lines represent linear regression for each of the study sites, while the solid line represents a one to one relationship for reference.

2.3.4 Crown Growth

Individual tree crown growing was only validated for correctly detected trees. Of the tested crown growing methods, all but one consistently underestimated the crown area, while the lidR watershed method tended to have a slight overestimation error (Table 2.5). Overall, the lidR watershed method provided the smallest crown area bias at 3.68 and 1.40 m^2 at KNF and MEF, respectively. Comparing the observed and lidR watershed extracted crown areas showed the method's tendency to slightly overestimate small crowns and slightly underestimate larger crowns (Figure 2.7). These errors in crown area translate to slight overprediction bias in crown radius for the lidR watershed method, with a crown radius RMSE of 0.76 and 0.65 m at the KNF and MEF study sites, respectively (Table 2.5). The lidR watershed

methods correctly extracted 41% of crown radii to within 0.25 m and 64% to within 0.50 m. In addition to tree-to-tree accuracies, the different methods were evaluated for the accuracy of their total extracted canopy area. Total lidR watershed extracted crown area was under by 24.8% of the observed 2,530 m^2 at KNF and 13.3% of the observed 1,483 m^2 at MEF, compared to the other methods that underestimated by 35.0-44.3% (Table 2.5). While some of the other evaluated methods performed similarly for an individual metric, none of these methods consistently minimized bias and precision as well as the lidR watershed method.

Table 2.5. Assessment of the crown growing methods ability to characterize individual tree crown area and radius for only extracted trees, as well as total extracted crown area error as a proportion of field observed crown area.

	Crown Growing Method	KNF	MEF
Crown Area Mean Error (m^2)	lidR Watershed	3.68	1.40
	ForestTools MCWS	-4.61	-2.14
	lidR Dalponte	-7.30	-4.04
	lidR Silva	-7.48	-4.01
Crown Area RMSE (m^2)	lidR Watershed	16.53	10.45
	ForestTools MCWS	15.80	8.1
	lidR Dalponte	15.85	9.58
	lidR Silva	16.03	9.74
Crown Radius Mean Error (m)	lidR Watershed	0.21	0.09
	ForestTools MCWS	-0.31	-0.16
	lidR Dalponte	-0.44	-0.26
	lidR Silva	-0.43	-0.24
Crown Radius RMSE (m)	lidR Watershed	0.76	0.65
	ForestTools MCWS	0.83	0.54
	lidR Dalponte	0.83	0.61
	lidR Silva	0.82	0.61
Total Crown Area Error (%)	lidR Watershed	-24.8%	-13.3%
	ForestTools MCWS	-35.0%	-37.6%
	lidR Dalponte	-44.3%	-41.6%
	lidR Silva	-44.3%	-42.2%

2.4 Discussion

2.4.1 Tree Detection and Crown Growing Performance

This study evaluated three individual tree detection algorithms with 97 different parameterizations at two study sites to identify the best strategy for detecting trees in complex uneven-aged ponderosa pine forest structures. The best performing parameterization provided Overall tree detection accuracies of 78.8% at KNF and 68.7% at MEF. Standard ITD methods performed on LiDAR or SfM-derived CHM have detected real trees on site with accuracies ranging from 40% to 90% (Heurich et al., 2008; Maturbong et al., 2019; Persson et al., 2002). The wide range of successful tree matching can be attributed to variation in forest structures, the methods tested, and the size of trees included for analysis (Zhen et al., 2016). However, the present study evaluated these methods across a comprehensive range of tree structures, unlike many studies that target only overstory trees (Zhen et al., 2016). The Overstory tree detection accuracy in this study was 97.2% and 93.9% at KNF and MEF, respectively, which is on the higher end of what has been previously reported in the literature (Belmonte et al., 2019; Yu et al., 2011). The high Overstory detection accuracy might be attributed to the use of variable window equations as opposed to the more common fixed window approach.

More recent literature has determined F-score to be a more holistic measure of validation as it integrates the true positive, false positive, and false-negative rates. Our best Overall F-scores were 0.57 and 0.58 at KNF and MEF, respectively; the accuracy of performance in the Overstory produced F-scores of 0.71 and 0.75 at KNF and MEF, respectively, which is in line with more recent ITD studies that have found F-scores ranging from 0.74 - 0.94 (Mohan et al., 2017; Silva et al., 2016). The difference in accuracies can be explained by variations in the

stringency of accuracy assessments and what trees were included in each study. This study utilized nearly 5,000 trees from stem-mapped sites with rigorous tree level matching to determine true positive detections (i.e., 3 m horizontally and 10% of field height). Mohan et al. (2017) matched detected trees with real trees through a visual assessment that identified 367 trees and resulted in an F-score of 0.86, but only visually discernible trees from the imagery were included. More rigorously, Silva et al. (2016) achieved an F-score of 0.83 by applying a similar tree-based matching logic to that used in this study but allowed trees to be matched with a location error of up to 10 m to accommodate GPS errors and only tested forest densities up to 200 trees per hectare. Given that each of these studies only evaluated the ability of local-maximum, fixed-window detection strategies to observe dominant tree structures, it is promising to see that the current study was able to provide similar results in the Overstory while maintaining reasonable detection throughout all tree size classes.

Of the tested individual tree detection methods, linear models used in the variable-window function provided the 18 top-performing outputs at MEF and 10 at KNF. Despite the consistently high performance of the linear models, the best exponential models were similar in performance. While this study examined a variety of models, the consistently high F-scores found through the top 20 models at both sites point to some flexibility in model coefficients that provide reasonable results in the Overstory and Intermediate stratums (Figure 2.8). However, when considering the entire forest canopy as all trees > 1.37 m tall, this coefficient space narrows for both the linear and exponential model to the smallest intercept values of 0.4 with a higher slope term around 0.07 (Figure 2.8). This combination of coefficients provides a sufficiently small search window in the Understory to identify smaller, more densely located

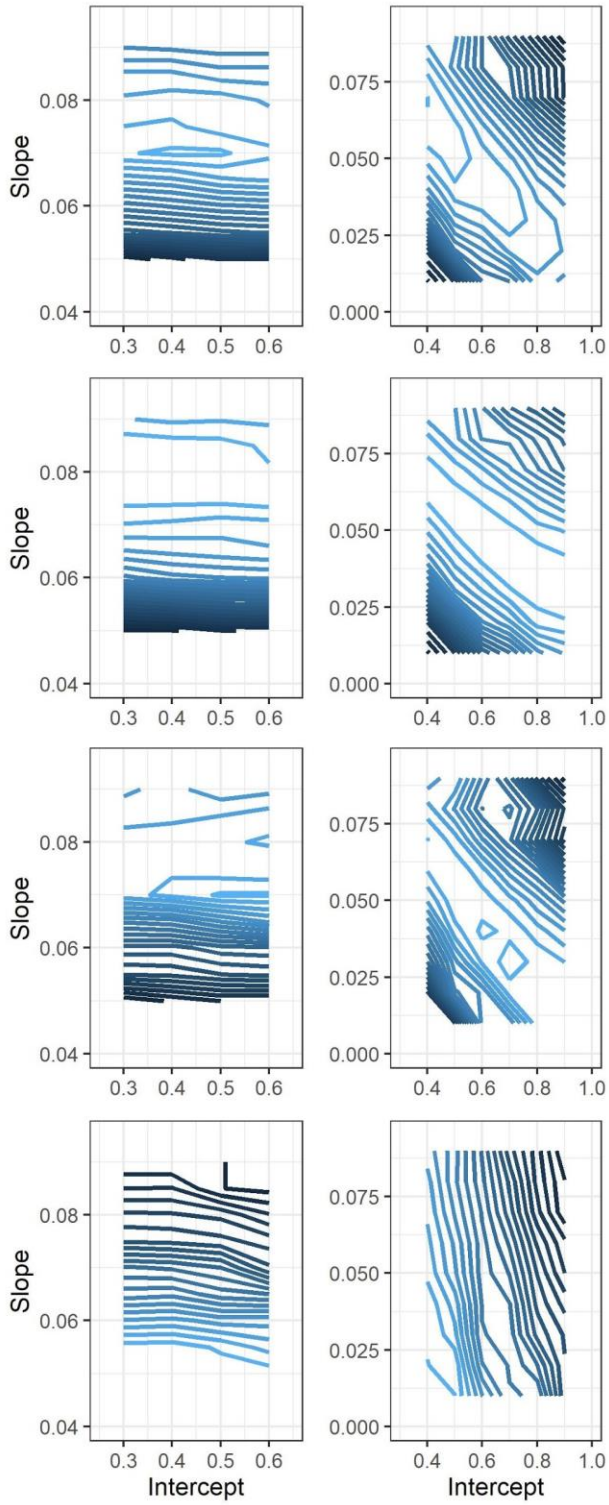

Figure 2.8. Contour plot of F-scores based on linear (left panels) and exponential (right panels) model coefficients, with higher F-scores indicated by lighter shades of blue. F-scores have been averaged across the two study sites for each set of unique model coefficients and are arranged top to bottom as Overall, Overstory, Intermediate, and Understory strata.

trees while scaling the search window to be large enough not to segment individual tree crowns in the Overstory stratum. The variation in F-score values across the canopy strata and Overall point to a need for future investigations to consider adaptive variable window functions such as piecewise regression so that more consistent accuracies can be achieved across all tree sizes.

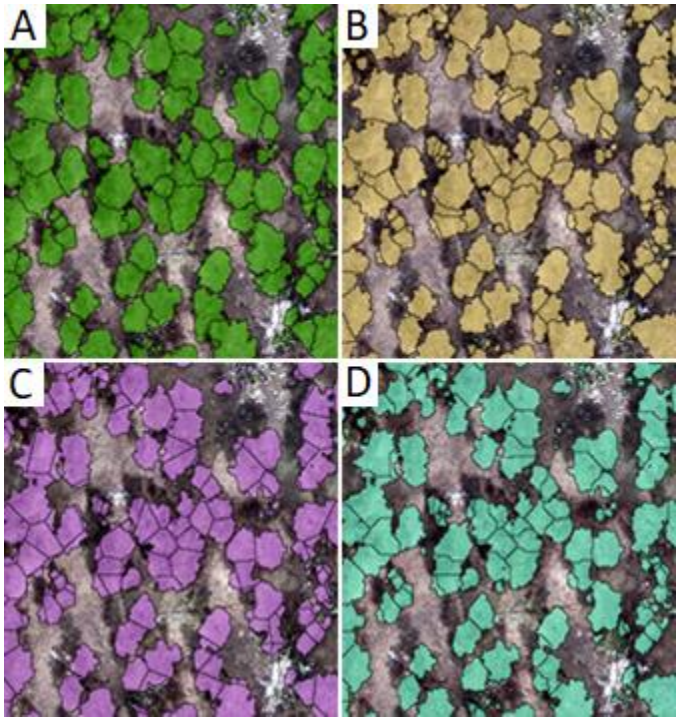

Figure 2.9. Visual representation of the four crown growing methods: (A) lidR watershed, (B) ForestTools marker-controlled watershed, (C) lidR Silva, and (D) lidR Dalponte.

Crown area mean error across all methods ranged from -7.48 to 3.68 m^2 at KNF and -4.04 to 1.40 m^2 at MEF (Table 2.5). The lidR watershed method performed the best overall and produced a more natural crown representation, most likely due to its decision-making process on a pixel-by-pixel level (Figure 2.9). Silva and Dalponte both utilize geometric processes that produced straight lines and hard edges in crown groupings.

With a study CHM resolution of 0.25 m, crown area mean error can be described as a bias of -30 to 15 pixels at KNF and -16 to 6 pixels at MEF. Crowns present at KNF were, on average, much larger than crowns present at MEF. Therefore, the smaller pixel size may have helped to mitigate error that could have been present with a larger pixel size ≥ 0.5 m. Crown radius RMSE across all methods ranged from 0.76 to 0.82 at KNF and 0.55 to 0.65 at MEF. This study's precision in extracted crown radii slightly improves on those found in Panagioditis et al. (2017), who found a crown diameter RMSE of 0.82 and 1.04 m for two study sites. This difference in accuracy may be attributed to Panagioditis et al. (2017) working in a typically higher canopy cover forest system. However, their assessment was restricted to trees > 12 m tall, and they only used observed tree locations to initiate the crown segmentation procedure. Since crowns were grown in our study from the detected tree X and Y coordinates, there were instances where measured trees in the field were not correctly matched with detected trees. This error was restricted in calculating crown area and radii errors at the individual tree level but could explain the positive bias in our best performing method. Additionally, the total crown area was directly compared regardless of if a tree was detected or omitted. This omission error propagated through to cause an underestimation of the total crown area across methods from -44.3% to -24.8% at KNF and -33.2% to -13.3% at MEF (Table 2.5).

2.4.2 Omission Modeling

This study's use of large stem-mapped study sites provided nearly 5,000 trees for validation and evaluation of how forest structure impacts the probability of detecting a tree. Logistic regression results underscore the importance of local neighborhood forest structure on the detection probability of an individual tree. The evaluation of how forest structure interacts

with a tree's size may provide insights into the potential applications for which moving window individual tree detection is best suited.

The best performing ITD methods maintained similar tree height distributions and closely matched the total number of trees in the Overstory and Intermediate strata (Figure 2.4). The large omission error for Intermediate stratum trees at KNF is likely attributed to the site's greater vertical heterogeneity and these trees tending to occur in local neighborhoods with greater basal area than were seen at MEF. This is supported by the logistic regression that found the trees most likely to be missed in these strata were in dense tree groups at the higher end of the observed local basal area and tended to be at least 20% shorter than neighboring trees (Figure 2.5). The relatively high basal areas seen in these sites are indicative of untreated ponderosa pine forest conditions (Tinkham et al., 2016) and indicate that UAS single tree monitoring performance should increase in post-treatment environments for dominant and codominant trees.

Although relative distributions of heights were maintained between observed and detected trees, Understory trees experienced variable under-detection rates with 86 and 48% of trees being identified at KNF and MEF, respectively (Table 2.5). The differences between these sites in correctly identifying Understory canopy stratum trees can be attributed to MEF appearing to be in a stand re-initiation phase that has resulted in very high densities of small trees. Logistic regression identified that Understory trees in close proximity to other trees and relatively shorter than neighboring trees were much less likely to be detected (Figure 2.6). This under-detection of Understory trees most likely propagates through the crown growing, where

the crowns of smaller trees are under segmented, which results in a positive bias in the estimated crown area for smaller trees (Figure 2.7).

2.4.3 Applications in Forest Monitoring

Individual tree detection methods might be better suited for monitoring certain aspects of forest structure than traditional plot-level methods, which average out variation across larger scales. Due to the fine-scale nature of ecological processes that happen within forested ecosystems, capturing variation at the tree-to-tree, local neighborhood, and stand-level is crucial for understanding forest structural dynamics at any scale. Local and neighborhood interactions take place in three-dimensional space; therefore, understanding the vertical heterogeneity and complexity of a landscape can only be enabled through accurate monitoring of tree heights and relative locations. The best approach to accuracy validation would then rely on a large sample of observed and measured tree attributes.

While many studies of individual tree detection have stem-mapped validation data, it is more often plot-sampling gathered specifically for the study and is not comprehensive across the landscape being observed (Belmonte et al., 2019; Heurich et al., 2008)). Ponderosa pine forest management encourages heterogeneity in neighborhood forest structure, which may lead to sampling plots overlooking the variation in density (Addington et al., 2018). The use of large, established, and longitudinal study plots further strengthens the relationship found between the effectiveness of ITD methods and observed forest structure. Large monitoring plots provide continuous coverage which can accurately capture the range of variability present on the landscape, something that smaller sampling plots may overlook. While most ITD method validation uses stem-mapped trees to some degree, it is important to evaluate potential flaws.

Larger trees on the landscape are known to have a disproportionate impact on their surrounding ecosystem and store a large amount of above-ground biomass in forest systems, accounting for nearly half of on-site AGB in some studies (Ligot et al., 2018; Sist et al., 2014). Variation in large tree density has been found to increase understory microclimate variation, which can influence regeneration dynamics in certain conifer systems (Ma et al., 2010). Because of the importance of these trees for carbon management and monitoring, the reliable distribution of overstory trees produced through UAS-photogrammetry derived ITD methods could be a powerful sampling tool, both at the stand and landscape level. Coupling ITD methods with the relative high precision of crown growing methods could provide valuable information to forest managers. Crown growing methods could also identify trees without crowns and help identify snags, which serve as wildlife habitat, influence shaded microclimates, and perpetuate forest openings. Reliable characterization of tree height and crown area could enable cheaper and more accessible drone monitoring technology to provide observations of carbon storage in low productivity forest systems.

While it may only be possible to fully characterize the density, location, and height distribution of smaller trees in a post-treatment condition, the representation of relative height distributions may hold promise for other ecological applications. Forest structural variation across size classes has far-reaching consequence for ecological processes happening across scales. The spatial pattern and density of trees influence the presence of shade-tolerant and -intolerant plants present on the landscape beyond trees. While shading by the intermediate and overstory canopy in ponderosa pine forests can promote establishment of shade-tolerant species such as Douglas-fir (*Pseudotsuga menziesii* (Mirb.) Franco; Cannon et al., 2016),

substantially altering fire disturbance dynamics within this system. These ITD methods could be coupled with concepts of tree approximate objects to describe ecologically important forest structures (Jeronimo et al., 2018), particularly when approximations of forest structure are often enough for planning and decision-making processes. Understanding the spatial configuration of tree patch sizes and forest openings through UAS monitoring would provide the detail needed for restoring ponderosa pine forest pattern and structure. Implementing methods to distinguish between live and dead trees within individual tree detection may also prove useful, as standing dead trees can function as nesting habitat for some bird species (Vogeler et al., 2016).

Most ponderosa pine-dominated forests within the central and southern Rocky Mountains that have intact disturbance regimes or have undergone restoration have local basal areas of <4.6 to 18.4 m^2 (Addington et al., 2018). With these being such lower stand basal area levels than are currently seen across most of the KNF and MEF study areas, there is reason to believe that UAS single tree methods would perform better across all tree sizes when monitoring post-treatment forest conditions. Given the increased temporal resolution of UAS monitoring, repeated observations in post-treatment conditions could contribute to further understanding of forest stand dynamics such as seedling establishment, seedling and juvenile mortality, and the role of larger trees and gaps for propagating regeneration. Further investigation is needed to evaluate these methods for monitoring treated environments and to assess the full range of forest inventory attributes that UAS single tree analysis can provide.

2.4.4 Study Limitations

Our stem-mapped tree locations are highly accurate through the use of an independent grid system that does not rely on taking GPS locations of trees, a practice that can be inaccurate due to canopy interference with satellite reception. This allows for a relatively high degree of accuracy in matching trees, as new trees are recorded into the grid through relative positioning to the oldest trees to mitigate the propagation of error throughout survey years. Despite having a high degree of horizontal precision, matching detected trees to stem-mapped trees at KNF was challenging due to potential error in field measurements. While field observations of tree height are the current standard, they are typically negatively biased by 5% and vary in precision by 10% (Vastaranta et al., 2009). This negative bias in field height might account for the shift in heights between the distributions of KNF field and ITD heights (Figure 2.4). Current literature suggests that drone photogrammetry provides similar accuracies in describing tree heights as LiDAR and field-based measurements (Tang and Shao et al., 2015; Tiberiu Paul Banu et al., 2016). Detected heights at KNF were matched to field measured heights using an MHD of 5 m due to potential difficulty in obtaining accurate field observations of heights in high canopy cover (Andersen et al., 2006).

The variable errors in the crown growing methods can be attributed to several factors. The high under-detection rate of Understory trees led to a single detected tree being attributed with the crown area of several neighboring small trees. In contrast, larger trees that were accurately detected were occasionally overly segmented due to forked treetops, which led to large disparities between observed and detected crown areas. Errors also exist in our ability to reliably characterize crown areas in the field through the use of two crown diameter

observations. This technique assumes that a tree's crown area is a perfect ellipse and that there is no error in determining the two ellipse diameters. While not a perfect relationship, the relatively strong correlation ($r > 0.69$) seen between detected and observed crown area indicates that the UAS observed crown areas provide reasonable approximations.

2.5 Conclusion

This study found that photogrammetry-based ITD methods perform as well, if not better, than comparable LiDAR-based ITD methods. The high-resolution CHM provided by UAS SfM data allows for accurate tree-level crown growth, with the potential for more accurate results when observed tree locations are used. Our work establishes that adaptive variable-window strategies increase tree detection rates across the full range of tree sizes. Such characterization of tree-level forest structure distributions would be valuable for monitoring changes in forest structure from pre- to post-disturbance. Further work should explore if the accuracy we observed for UAS-based ITD methods using variable window functions translates to other forest systems.

Works Cited

Addington, Robert N., et al. *Principles and Practices for the Restoration of Ponderosa Pine and Dry Mixed-Conifer Forests of the Colorado Front Range*. p. 129.

Andersen, Hans-Erik, et al. "A Rigorous Assessment of Tree Height Measurements Obtained Using Airborne Lidar and Conventional Field Methods." *Canadian Journal of Remote Sensing*, vol. 32, no. 5, 2006, p. 12.

Andrew Plowright (2018). ForestTools: Analyzing Remotely Sensed Forest Data. R package version 0.2.0.

Andrew Romain (2020). lidR: Airborne LiDAR Data Manipulation and Visualization for Forestry Applications. R package version 2.2.5

Balsi, M., et al. "Single-Tree Detection in High-Density LiDAR Data from UAV-Based Survey." *European Journal of Remote Sensing*, vol. 51, no. 1, Jan. 2018, pp. 679–92. *DOI.org (Crossref)*, doi:10.1080/22797254.2018.1474722.

Belmonte, Adam, et al. "UAV -derived Estimates of Forest Structure to Inform Ponderosa Pine Forest Restoration." *Remote Sensing in Ecology and Conservation*, edited by Ned Horning and Stephanie Bohlman, Dec. 2019, p. rse2.137. *DOI.org (Crossref)*, doi:10.1002/rse2.137.

Cannon, Jeffery B., et al. "Variability in Mixed Conifer Spatial Structure Changes Understory Light Environments." *Forests*, vol. 10, no. 11, Nov. 2019, p. 1015. *DOI.org (Crossref)*, doi:10.3390/f10111015.

Chava, J., Davies, S.J., Phillips, O.L., Lewis, S.L., Sist, P., Schepaschenko, D., Armston, J. Baker, T.R., Coomes, D., Disney, M., Duncanson, L., Hérault, B., Labrière, N., Meyer, V., Réjou-

Méchain, M., Scipal, K., and Saatchi, S. 2019. Ground data are essential for biomass remote sensing missions. Surveys in Geophysics, vol. 40, p. 863-880, *DOI.org (Crossref)*, doi:10.1007/s10712-019-09528-w.

Churchill, Derek J., et al. "Restoring forest resilience: from reference spatial patterns to silvicultural prescriptions and monitoring." *Forest Ecology and Management* 291 (2013): 442-457.

Dalponte, Michele, and David A. Coomes. "Tree-Centric Mapping of Forest Carbon Density from Airborne Laser Scanning and Hyperspectral Data." *Methods in Ecology and Evolution*, edited by David Murrell, vol. 7, no. 10, Oct. 2016, pp. 1236–45. *DOI.org (Crossref)*, doi:10.1111/2041-210X.12575.

"Detecting and Measuring Individual Trees Using an Airborne Laser Scanner." *PHOTOGRAMMETRIC ENGINEERING*, p. 8.

Dickinson, Yvette, et al. "Have We Been Successful? Monitoring Horizontal Forest Complexity for Forest Restoration Projects: Monitoring Horizontal Forest Complexity." *Restoration Ecology*, vol. 24, no. 1, Jan. 2016, pp. 8–17. *DOI.org (Crossref)*, doi:10.1111/rec.12291.

Fraser, Benjamin, and Russell Congalton. "Issues in Unmanned Aerial Systems (UAS) Data Collection of Complex Forest Environments." *Remote Sensing*, vol. 10, no. 6, June 2018, p. 908. *DOI.org (Crossref)*, doi:10.3390/rs10060908.

Goutte, Cyril, and Eric Gaussier. "A probabilistic interpretation of precision, recall and F-score, with implication for evaluation." *European conference on information retrieval*. Springer, Berlin, Heidelberg, 2005.

Heurich, Marco. “Automatic Recognition and Measurement of Single Trees Based on Data from Airborne Laser Scanning over the Richly Structured Natural Forests of the Bavarian Forest National Park.” *Forest Ecology and Management*, vol. 255, no. 7, Apr. 2008, pp. 2416–33. *DOI.org (Crossref)*, doi:10.1016/j.foreco.2008.01.022.

Jeronimo, Sean M. A., et al. “Applying LiDAR Individual Tree Detection to Management of Structurally Diverse Forest Landscapes.” *Journal of Forestry*, vol. 116, no. 4, June 2018, pp. 336–46. *DOI.org (Crossref)*, doi:10.1093/jofore/fvy023.

Kaartinen, Harri, et al. “An International Comparison of Individual Tree Detection and Extraction Using Airborne Laser Scanning.” *Remote Sensing*, vol. 4, no. 4, Mar. 2012, pp. 950–74. *DOI.org (Crossref)*, doi:10.3390/rs4040950.

Li, Wenkai, et al. “A New Method for Segmenting Individual Trees from the Lidar Point Cloud.” *Photogrammetric Engineering & Remote Sensing*, vol. 78, no. 1, Jan. 2012, pp. 75–84. *DOI.org (Crossref)*, doi:10.14358/PERS.78.1.75.

Ligot, Gauthier, et al. “The Limited Contribution of Large Trees to Annual Biomass Production in an Old-Growth Tropical Forest.” *Ecological Applications*, vol. 28, no. 5, July 2018, pp. 1273–81. *DOI.org (Crossref)*, doi:10.1002/eap.1726.

Lutz, James A. “The Evolution of Long-Term Data for Forestry: Large Temperate Research Plots in an Era of Global Change.” *Northwest Science*, vol. 89, no. 3, Aug. 2015, pp. 255–69. *DOI.org (Crossref)*, doi:10.3955/046.089.0306.

Lydersen, Jamie M., et al. “Quantifying Spatial Patterns of Tree Groups and Gaps in Mixed-Conifer Forests: Reference Conditions and Long-Term Changes Following Fire

Suppression and Logging." *Forest Ecology and Management*, vol. 304, Sept. 2013, pp. 370–82. *DOI.org (Crossref)*, doi:10.1016/j.foreco.2013.05.023.

Ma, Siyan, et al. "Spatial variability in microclimate in a mixed-conifer forest before and after thinning and burning treatments." *Forest Ecology and Management* 259.5 (2010): 904-915.

Maturbong, Bonifatius, et al. "Forest Inventory Sensivity to UAS-Based Image Processing Algorithms." *Annals of Forest Research*, vol. 0, no. 0, July 2019. *DOI.org (Crossref)*, doi:10.15287/afr.2018.1282.

Mielcarek, Miłosz, et al. "Testing and Evaluating Different LiDAR-Derived Canopy Height Model Generation Methods for Tree Height Estimation." *International Journal of Applied Earth Observation and Geoinformation*, vol. 71, Sept. 2018, pp. 132–43. *DOI.org (Crossref)*, doi:10.1016/j.jag.2018.05.002.

Mlambo, Reason, et al. "Structure from Motion (SfM) Photogrammetry with Drone Data: A Low Cost Method for Monitoring Greenhouse Gas Emissions from Forests in Developing Countries." *Forests*, vol. 8, no. 3, Mar. 2017, p. 68. *DOI.org (Crossref)*, doi:10.3390/f8030068.

Mohan, Midhun, et al. "Individual Tree Detection from Unmanned Aerial Vehicle (UAV) Derived Canopy Height Model in an Open Canopy Mixed Conifer Forest." *Forests*, vol. 8, no. 9, Sept. 2017, p. 340. *DOI.org (Crossref)*, doi:10.3390/f8090340.

Panagiotidis, Dimitrios, et al. "Determining Tree Height and Crown Diameter from High-Resolution UAV Imagery." *International Journal of Remote Sensing*, vol. 38, no. 8–10, May 2017, pp. 2392–410. *DOI.org (Crossref)*, doi:10.1080/01431161.2016.1264028.

Persson, Asa, Johan Holmgren, and Ulf Soderman. "Detecting and measuring individual trees using an airborne laser scanner." Photogrammetric Engineering and Remote Sensing 68.9 (2002): 925-932.

Popescu, Sorin C. “Estimating Biomass of Individual Pine Trees Using Airborne Lidar.” *Biomass and Bioenergy*, vol. 31, no. 9, Sept. 2007, pp. 646–55. *DOI.org (Crossref)*, doi:10.1016/j.biombioe.2007.06.022.

Popescu, Sorin C., et al. “Measuring Individual Tree Crown Diameter with Lidar and Assessing Its Influence on Estimating Forest Volume and Biomass.” *Canadian Journal of Remote Sensing*, vol. 29, no. 5, 2003, p. 14.

Popescu, Sorin C., Randolph H. Wynne, and John A. Scrivani. "Fusion of small-footprint lidar and multispectral data to estimate plot-level volume and biomass in deciduous and pine forests in Virginia, USA." *Forest Science* 50.4 (2004): 551-565.

Poznanovic, Aaron J., et al. “An Accuracy Assessment of Tree Detection Algorithms in Juniper Woodlands.” *Photogrammetric Engineering & Remote Sensing*, vol. 80, no. 7, July 2014, pp. 627–37. *DOI.org (Crossref)*, doi:10.14358/PERS.80.7.627.

R Core Team (2019). R: A language and environment for statistical computing. R Foundation for Statistical Computing, Vienna, Austria.

Silva, Carlos A., et al. “Imputation of Individual Longleaf Pine (*Pinus Palustris* Mill.) Tree Attributes from Field and LiDAR Data.” *Canadian Journal of Remote Sensing*, vol. 42, no. 5, Sept. 2016, pp. 554–73. *DOI.org (Crossref)*, doi:10.1080/07038992.2016.1196582.

Sist, Plinio, et al. “Large Trees as Key Elements of Carbon Storage and Dynamics after Selective Logging in the Eastern Amazon.” *Forest Ecology and Management*, vol. 318, Apr. 2014, pp. 103–09. *DOI.org (Crossref)*, doi:10.1016/j.foreco.2014.01.005.

Tinkham, Wade, et al. “Ponderosa Pine Forest Restoration Treatment Longevity: Implications of Regeneration on Fire Hazard.” *Forests*, vol. 7, no. 12, July 2016, p. 137. *DOI.org (Crossref)*, doi:10.3390/f7070137.

Torresan, Chiara, et al. “Forestry Applications of UAVs in Europe: A Review.” *International Journal of Remote Sensing*, vol. 38, no. 8–10, May 2017, pp. 2427–47. *DOI.org (Crossref)*, doi:10.1080/01431161.2016.1252477.

Vastaranta, Mikko, et al. *LASER-BASED FIELD MEASUREMENTS IN TREE-LEVEL FOREST DATA ACQUISITION*. p. 12.

Westoby, Matthew J., et al. "'Structure-from-Motion'photogrammetry: A low-cost, effective tool for geoscience applications." *Geomorphology* 179 (2012): 300-314.

Wulder, Michael A., et al. “Lidar Sampling for Large-Area Forest Characterization: A Review.” *Remote Sensing of Environment*, vol. 121, June 2012, pp. 196–209. *DOI.org (Crossref)*, doi:10.1016/j.rse.2012.02.001.

Yu, Xiaowei, et al. "Predicting individual tree attributes from airborne laser point clouds based on the random forests technique." *ISPRS Journal of Photogrammetry and remote sensing* 66.1 (2011): 28-37.

Zhen, Zhen, et al. “Trends in Automatic Individual Tree Crown Detection and Delineation—Evolution of LiDAR Data.” *Remote Sensing*, vol. 8, no. 4, Apr. 2016, p. 333. *DOI.org (Crossref)*, doi:10.3390/rs8040333.

Appendix

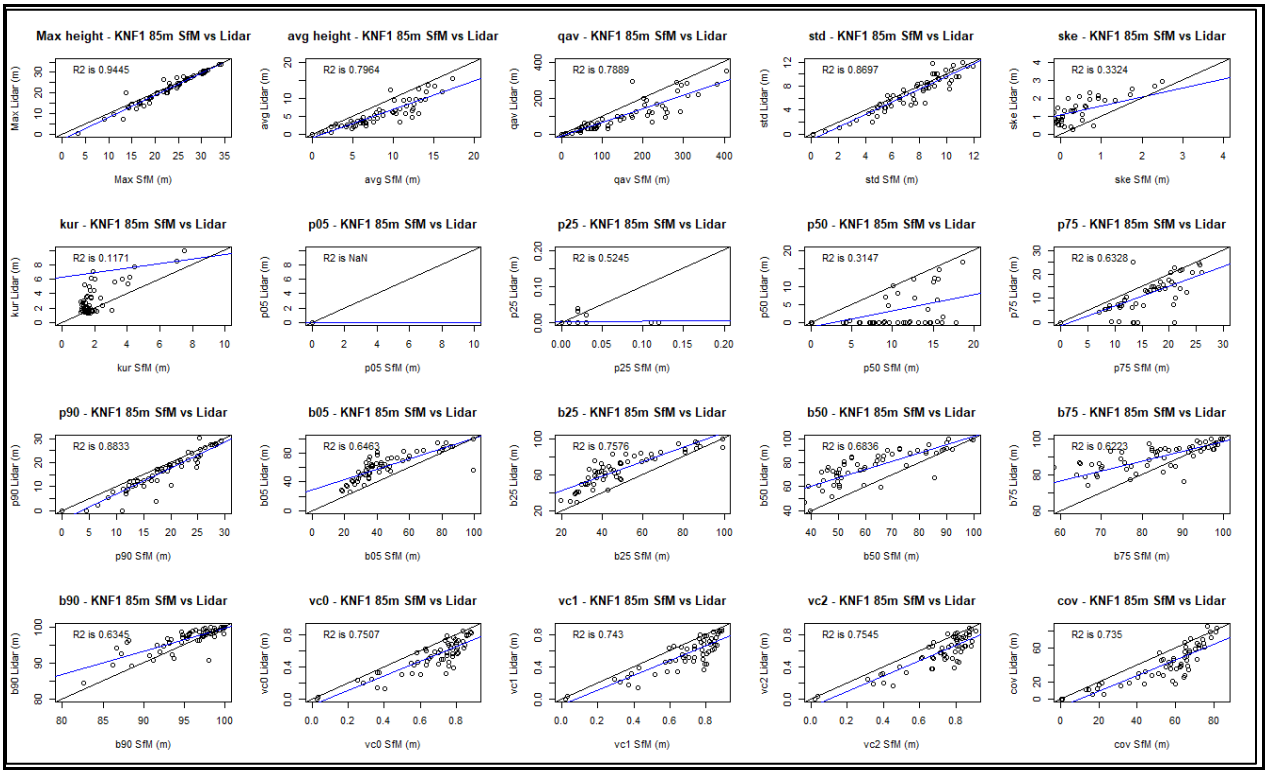

Supplemental Figure 1.1: LiDAR vs SfM point cloud structural metric comparisons for the model with the highest improved variance compared to LiDAR, which was the 85 m AGL altitude at KNF1, which had an improved variance of 26.3% over the LiDAR AGB model for that site.

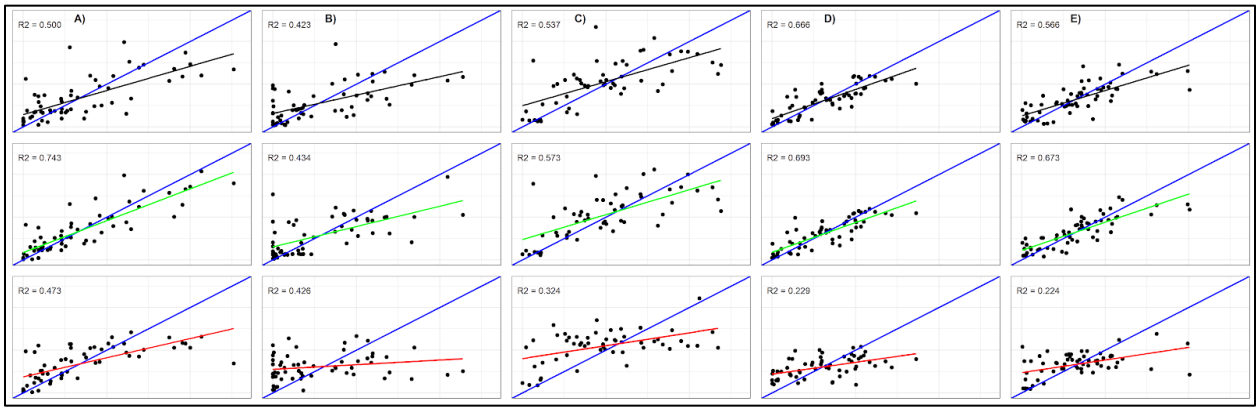

Supplemental Figure 1.2: Observed (x axis) vs Predicted (y axis) for KNF1 (A), KNF2 (B), KNF3 (C), MEF1 (D), and MEF2 (E) AGB models, representing from top to bottom the LiDAR (black line), highest altitude UAS (green line), and lowest altitude UAS (red line) models for each study area.

Supplemental Table 1.1. Agisoft Metashape processing parameters for SfM photogrammetry forest reconstruction.

Parameter	Setting
Align Photos	
Accuracy	Highest
Generic preselection	Yes
Reference preselection	Source
Reset current alignment	No
Key point limit	40,000
Tie Point Limit	4000
Apply masks to	None
Adaptive camera model fitting	Yes
Optimize Alignment	
Adaptive camera model fitting	Yes
Build Dense Cloud	
Quality	High
Depth Filtering	Mild
Calculate point colors	Yes
Calculate point confidence	No